Synthesis and Optimization of Quantum Dot-Based Technologies:

Solid-State Photovoltaics and Ferroelectric Particles

By

Toshia Lynn Wrenn

Dissertation

Submitted to the Faculty of the

Graduate School of Vanderbilt University

in partial fulfillment of the requirements

for the degree of

DOCTOR OF PHILOSOPHY

in

Chemistry

August, 2015

Nashville, Tennessee

Approved:

Sandra J. Rosenthal, Ph.D.

David E. Cliffel, Ph.D.

Janet Macdonald, Ph.D.

Yaqiong Xu, Ph.D.

ACKNOWLEDGEMENTS

TABLE OF CONTENTS

LIST OF FIGURES

CHAPTER I

INTRODUCTION

1.1 Semiconductor Nanomaterials

Nanomaterials have at least one dimension that is sub-100 nm, less than ten billionths of a meter. Within the nano- size regime, materials take on properties that are distinctly unique from their bulk counterparts. As the number of dimensions that are spatially confined increases, the more the charge carriers within the semiconductor are confined and the more pronounced the effects of the confinement. Based on dimensions, semiconductor nanomaterials are divided into three categories as seen in Figure 1.1.
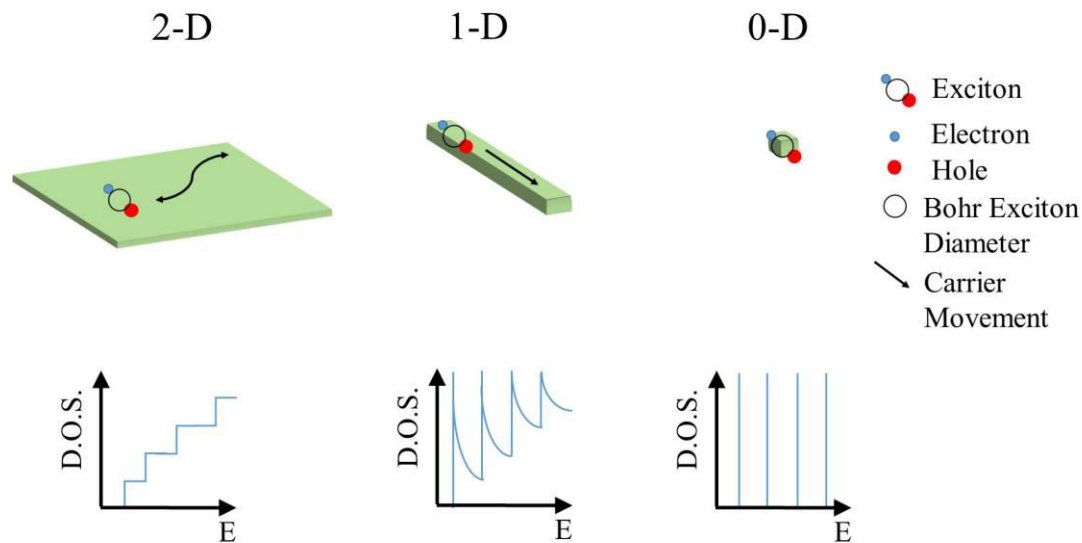
Figure 1.1 Impact of spatial confinement to 2 dimensions (2-D), 1 dimension (1-D), and 0 dimension (0-D) on carrier movement and the density of states (D.O.S.) on semiconductor nanomaterials

2-D semiconductor nanomaterials are spatially confined to the x-y plane, and the density of states for a 2-D semiconductor is dispersed in a stair-step pattern. Charge carriers may occupy a distribution of energies and migrate easily within the plane but only limitedly out-of-plane. The most widely utilized 2-D material is graphene, a semiconducting planar sheet of carbon atoms.

The confinement of graphene generates a unique band structure which can be tailored to generate a tunable bandgap ranging from zero to 0.25 eV bandgap. With a zero bandgap, graphene lacks an energetic barrier for conductivity, so graphene exhibits excellent in-plane conductivity. In light of its electrical characteristics, graphene is often incorporated into electric junctions and devices, including field-gated transistors and photovoltaics.

1-D nanomaterials are spatially confined in two dimensions; the density of states of 1-D materials is dispersed as spikes with exponential decay between each energy level. Charge carriers still occupy a distribution of energies but migration of carriers is more limited. The easiest 1-D nanomaterials to visualize are nanowires that are confined along the x- and y- axes and extend indefinitely in the z-direction. Confinement of nanowires limits charge transfer within the wire to a single direction, making nanowires effective charge-channeling agents. Another example of 1-D nanomaterials are porous networks. The networks spatially occupy three dimensions, but the pores typical extend into the material along a single axis. Increased porosity, the ratio of void volume to the volume of material, increases the exposed surface area of materials exponentially. The increased surface area increases the chemical reactivity of the material, which has led to the utilization of these as catalysts and gas-storage matrices.

0-D nanomaterials are particles that exhibit confinement in all three dimensions. The extreme confinement of these materials leads to extreme changes in the material properties. The density of states is quantized to discrete energy levels with carriers spatially confined in all directions. Like 1-D porous networks, confinement of particles in 3 dimensions leads to very high surface area, making nanoparticles effective catalysts as well. However, it is often the unique energetic and optic properties of 0-D semiconductors that are of interest for devices, especially alternative energy devices like photovoltaics.

1.2 Quantum Dots

Of particular interest to the current work are 0-D nanocrystals of semiconductors, more commonly known as quantum dots. An interesting juxtaposition exists between bulk semiconductors and quantum dots, especially in their electronic and optical properties. Bulk semiconductor materials exhibit an energy band structure that lies in between that of conductors and insulators. In conductor materials the valence and conduction bands overlap, resulting in highly mobile electrons and high conductivity. In insulator materials a large energy offset between the valence and conduction band exists, preventing conduction. The valence and conduction bands in semiconductors are offset by a small energy gap, known as the bandgap energy. While semiconductors are not always conductive like conductor materials, if enough energy is input into the system an electron and hole that are mobile and do not experience Coulombic interactions are generated. If the energy input into the system is slightly less than the bandgap, a bound electron-hole pair, known as an exciton, is generated. The difference between energy to generate an exciton and free carriers is the exciton binding energy. To balance the Coulombic interaction between the bound electron and hole, the exciton exhibits an equilibrium distance between the two charge carriers. This distance is known as the Bohr exciton diameter; often literature refers to the Bohr exciton radius, which is half the diameter distance. Quantum dots exhibit an energy band structure similar to their bulk counterparts; however, quantum dot energy band structure can be tuned.

In quantum dots the size of the material is reduced to less than the Bohr exciton diameter (shown in Figure 1.1), and the exciton energy is dictated by physical size of the particle rather than the Coulombic interactions.[1] This state is energetically unfavorable and requires more energy to stabilize. Thus as the size of the quantum dot restricts the separation distance of the

electron-hole pair of the exciton, the energy required to generate the exciton increases, resulting in size-tunable electronic and optical properties.[2]

As the size of semiconductor particles is decreased below the Bohr exciton diameter, an interesting quantization of the bandgap energy occurs, thus the name "quantum dots". Decreasing the size of the particle and increasing the spatial confinement of the exciton increases the energy of the excited state, leading to a decrease in the wavelength of light absorbed and emitted by the particles. L. Brus introduced the concept of quantum confinement in nanoscale semiconductors.[3] Brus modeled the energy quantization in semiconductor nanoparticles as:[3]

$$E_{ex} = \frac{\hbar^2 \pi^2}{2R^2}\left(\frac{1}{m_e}+\frac{1}{m_h}\right) - \frac{1.8e^2}{\varepsilon_2 R} + \frac{e^2}{R}\overline{\sum_{n=1}^{\infty}\alpha_n\left(\frac{S}{R}\right)^{2n}} \quad \text{(Eqn. 1.1)}$$

where E_{ex} is the difference in energy between the first excited level of the nanocrystal and the bulk bandgap, $\hbar$ is the quotient of Planck's constant over 2π, R is the particle radius, m_e and m_h are the effective masses of the electron and hole, respectively, e is the absolute charge of an electron, ε_2 is the dielectric constant of the semiconductor material, α_n is a constant that relates the dielectric constants of the semiconductor material and the surrounding medium,[3] and S is the wavefunction that describes the position of the electron and hole in the $1S$ exciton. The first term of Brus' equation describes the quantization energy of the electron-hole pair spacing and is reminiscent of Schrödinger's particle-in-a-box, in which the difference between energy levels is inversely related to the square of the length of the box. This energy of localization term is responsible for the observable blue shift in the optical properties of the particles. The second term is the Coulombic attraction of the oppositely charged carriers; it generates a small red shift in the optical properties. The third term is a perturbation of the electrons around the exciton.

4

1.3 Overview

Due to the unique size-tunability of the optical and electronic properties, quantum dots form the basis of many energy devices, including quantum dot-sensitized solar cells as described in the current work. However, development of devices using materials that are not visible to the naked eye requires novel techniques to both build the devices and to evaluate the quality of the materials and final devices. In the current manuscript, the techniques and characterization of an all solid-state quantum dot sensitized solar cell containing 1-D titanium dioxide nanotubes and 0-D quantum dots are described in part 1. In part 2, the manipulation of quantum dots to generate ferroelectric particles is described.

PART I: QUANTUM DOT-SENSITIZED SOLAR CELLS

CHAPTER II

INTRODUCTION

As the impact of man on the environment and climate becomes better understood, studies of alternative energy sources to alleviate the negative impact of mankind have become imperative.[4] It is indisputable that the most abundant natural resource is solar energy, so the growing prominence of devices which utilize this resource is unsurprising.[4] However while the sun provides enough power to meet global demand, the technology and means to efficiently capture and make use of this power remain elusive. One possible method of capturing solar energy is the use of photovoltaics (PVs). PVs are comprised of semiconductor materials that absorb the energetic photons from the sun resulting in the promotion of an electron from the material's valence band to its conduction band. The photo-excited electron and resulting hole are then swept out of the material in opposite directions into an external circuit to power a load. In order for the charge carriers to be separated and swept out of the semiconductor material, the architecture of the PV device must promote charge separation either through an inherent electric field (as is the case for silicon cells and heterojunction devices) or through energy resonance (as is the case for dye-sensitized cells and the cells presented in this research).[5]

While silicon cells dominate current PV markets, the cost and energy input during the production of these PVs limits their viability.[6] Due to rising demand in the photovoltaic market, the need to further investigate low-cost, low-energy-input PVs to subsidize or replace silicon solar cells is apparent.

2.1   Photosynthesis: Inspiration from Nature

Like many other aspects of science, nature provides a prominent example of an ideal system. Nature, through billions of years of evolutionary trials, has created the reaction centers and molecular wiring necessary to produce a 99% photon-to-electron production efficiency during photosynthesis.[7] For simplicity, we will follow the photosynthetic pathway of photosystem I. In photosystem I, photoexcited electrons within membrane-bound chlorophyll are transferred along their energy gradient to the P_{700} reaction center through two core chlorophyll. The electrons flow through an internal electron chain to pheophytin then to quinone, where they are transferred to a terminal iron-sulfur complex. The electrons are collected by ferredoxin for use in further photosynthetic reactions. The "vacant" hole is scavenged by soluble plastocyanin.[8] Photosynthesis owes its high quantum efficiency to two core concepts: 1. Rapid transport of the photoexcited electron wherein extraction across the thylakoid membrane occurs in less than 1 μs[8], and 2. Physical and energetic separation of the charge carriers. An ideal solar cell architecture would capitalize on these concepts while also containing readily-accessible, low energy-input materials. For mankind to fully-achieve an energetically efficient solar cell, a device architecture mimicking nature's integrated system of molecular engineering and effective light harvesting and charge extraction is needed. Quantum dot-sensitized solar cells, which emulate the architecture proposed by Grätzel in 1991 for dye-sensitized solar cells[9], meet the above requirements.

2.2   Solar Cells

2.2.1   Traditional silicon p-n junction

The most common and commercially- available solar cells are silicon p-n junction cells. Silicon p-n junction cells contain two layers of doped silicon. The n-type layer is doped with a material such as phosphorus, which donates extra negative electrons to the structure. The p-type layer is doped with a material such as boron, which donates extra positive holes to the structure. When the two layers are placed in contact with one another, the extra charges at the junction and for some depth (d) into the layers combine. The result is a charge-depleted region with the length of 2d. On the n-type side a seemingly positive barrier is established; on the p-type side a seemingly negative barrier. When the silicon within the depleted region is photo-excited by a photon with energy in excess of silicon's bandgap, the excited electron and resultant hole are quickly swept apart by the inherent electric field generated by the charge barriers on either side of the region. If the charge carriers diffuse effectively through the region, the carriers are swept through the external silicon layers into an external circuit to do work.

With the surge of silicon solar cells from China driving the cost of solar cells to all-time lows, the economic benefit of alternative solar cells is falling under scrutiny. However, while the financial benefits of the inexpensive materials used to fabricate alternative solar cells have been expounded as an advantage, the need for and long-term benefits extend beyond economic considerations.

To fully-understand the environmental benefits of alternative solar cells, an assessment of the negative impact and costs of silicon solar cell fabrication must be considered. Silicon is the most common element after oxygen within the earth's crust, so utilization of such a readily-available material seems ideal. However, as-harvested-silicon is not viable for use in solar cells.

It must undergo Siemen's purification to reach a level of purity conducive to efficient energy production and collection[10]. Siemen's purification is a minimum of 18 high energy-input steps, whose by-products are large quantities of hazardous chemicals such as silicon tetrachloride, which is highly toxic and corrosive. In fact, the purification process is so energy consuming, the Hemlock Semiconductor Group (Hemlock, MI) which purifies silicon for use in solar cells and electronics, reported in 2013 that at 420 MWs its energy-usage was the highest for any single-site energy consumer in Michigan[11]. This energy-requirement is for the operation of the purification plant only, it does not include the energy required to fabricate the actual solar cells.

In addition to costly initial purification of the solar cell materials, silicon solar cells have a limited photoactive region and energy collection capability. Bulk silicon has an indirect bandgap of 1.1 eV, which limits its ability to effectively harness the energy of the solar spectrum. In addition to the bandgap energy limitation, the molar extinction coefficient for silicon at the bandgap[12] is 1.30×10^{-5} eV, which means of photons that exceed the bandgap only a very small portion are absorbed within the pathlength of the silicon devices. Beyond the physical limitations of silicon, utilization of it within a bulk *p-n* junction places a thermodynamic limit on the energy efficiency of about 30%, commonly referred to as the Shockley-Queisser limit.[13] Some progress in overcoming these limitations has occurred by utilizing micro-patterned Si as artificial photosynthesis systems,[14] sliver cells,[15] polycrystalline devices,[16] and solar energy concentrators;[17] however, large-scale production of Si solar cells still relies on purified precursors assembled into bulk junctions.

2.2.2 Dye-sensitized solar cells

In 1991, O'Reagan and Grätzel proposed the novel solar cell architecture depicted in Figure 2.1.[9] The key features of the Grätzel cell are the low-cost, easily produced materials and its relatively high solar power efficiencies. The materials consist of an electron collector of colloidal titanium dioxide (TiO_2) particle network, a light harvester of sensitized with Ru-based dye, a hole- scavenging iodide/triiodide electrolyte, and contact electrodes. The electron conductor TiO_2 is a relatively inexpensive, readily available material, frequently used in household products such as make-up and paint. However, the Ru-based dyes and iodide/triiodide electrolyte are not as inexpensive and are responsible for the majority of the material costs associated with dye-sensitized solar cells.[18]

The key mechanistic feature of dye-sensitized solar cells is the separation of carrier transport from carrier production; this separation reduces one of the most common causes of efficiency loss in solar cells, carrier recombination. By having electrons injected into the TiO_2 almost immediately upon generation and holes chemically scavenged by reduction of iodide to triiodide, recombination becomes unfavorable. In addition to the decrease in recombination of carriers, dye-sensitized solar cells maximize charge carrier generation by having large surface area of TiO_2 sensitized with dye molecules. Since, dye-sensitized solar cells depend on charge injection and percolation, rather than carrier drift as in silicon and thin film devices, thicker devices can efficiently harvest more light.
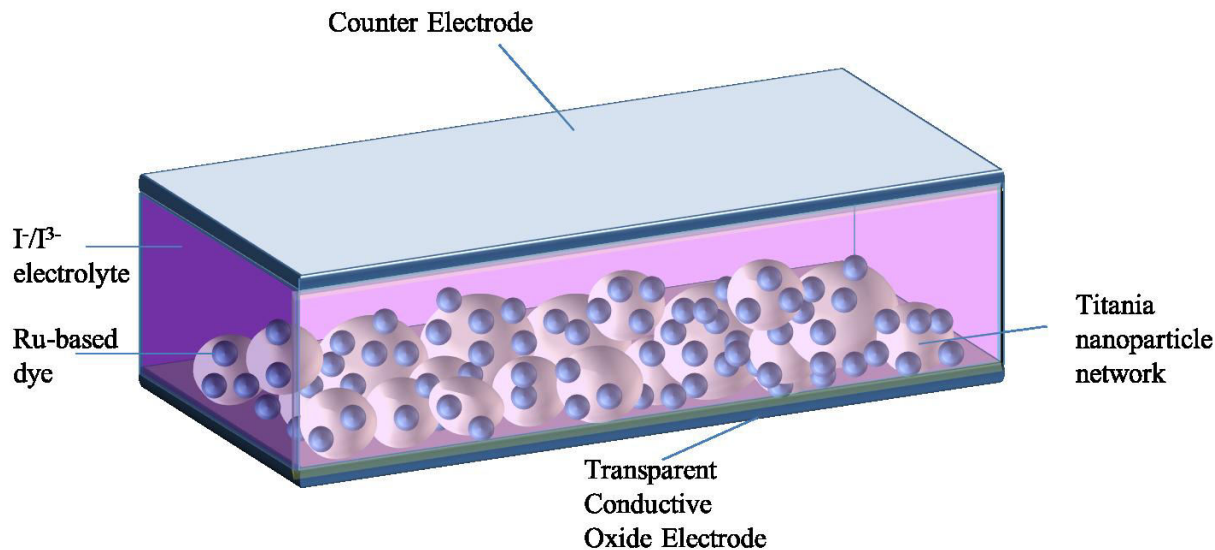
Figure 2.1 Illustration of major components of dye-sensitized solar cells

In recent years several studies have been conducted to enhance the efficiency of dye-sensitized solar cells through a variety of methods. These methods can be divided into three main categories: 1. Increase carrier production by increasing light absorption and 2. Increase electron lifetime within TiO_2 and 3. Reduce hazards and leakage associated with liquid electrolyte

The first category can be further subdivided into two categories: 1. Use of novel absorbing materials and 2. Increase of dye-loading. The use of novel absorbing materials spans from novel dyes, such as "black dye". The highest efficiency dye-sensitized solar cells make use of black dye, Ru-$(SCN)_3$- 4,4',4"-tricarboxy 2,2':6',2"-terpyridine, described in Nazeeruddin's work.[19]

However, the highest efficiency of 11.2% for dye-sensitized solar cells is only achieved by combining black dye with guanidinium thiocyanate, a self-assembly facilitating agent.[20] Use of a self-assembly facilitating agent allows the formation of a more compact dye monolayer increasing the amount of dye covering the available TiO_2 surface area thus increasing photon

absorption and efficiency. Another method of increasing efficient light harvesting is treating the

TiO_2 with $TiCl_4.$ [21] Treating the TiO_2 with $TiCl_4,$ improves binding of dye molecules to the TiO_2.

In attempts to further increase surface area of TiO_2 and to increase electron lifetime

within the TiO_2, numerous studies have been conducted replacing the TiO_2 network with TiO_2

nanotubes. Nanotube arrays can be produced by imprinting a sol-gel of TiO_2 with polymer molds

of anodic alumina nanotubes.[22] However, the arrays produced in this fashion required multiple

steps and often do not match the mold due to air trapped during the embossing process.

The more common technique for obtaining nanotube arrays is electrochemical oxidation

of titanium.[23] During electrochemical oxidation, a piece of titanium is exposed to typically a

fluoride-based electrolyte, although some new research has successfully produced nanotubes in

non-fluoride solutions such as perchloric acid[24] or combination of oxalic, formic, and sulfuric

acids with ammonium chloride.[25] The benefits of incorporating nanotubes into dye-sensitized

solar cells remain the same no matter the production method. The vertical orientation of the

nanotubes allows increased dye-loading as well as decreased electron percolation. In

nanoparticle networks only pores open to the exterior can be functionalized with dyes decreasing

the surface area available for sensitization. In nanotube arrays, theoretically the entirety of both

the inner and outer walls of the nanotubes can be sensitized with dye molecules resulting in an

increase in functionalizable-surface area. Also, the vertical orientation of the tubes promotes

unidirectional electron transfer to the anodic contact of the solar cell. In particle networks,

charges can become trapped in localized percolation limiting their mobility and ultimately their

observed lifetimes. In fact, electron lifetime in nanotube films are up to three orders of

magnitude higher than those in nanoparticle networks;[26] indicating longer nanotube arrays can be

effectively used to even further increase functionalizable surface area without loss of electrons through recombination.

Another common issue associated with dye-sensitized solar cells is leakage of the liquid electrolyte which can cause efficiency loss and be a potential health hazard (iodide/triiodide electrolytes have an acute toxicity rating of 4 and are known irritants to skin, eyes, and mucous membranes).[27] Hodes published an in-depth comparison of the recombination types and rates observed in dye-sensitized and semiconductor-sensitized solar cells[28] in which he reports that within a system with a solid hole-conducting material the hole-injection rate from the light-harvester is 6 orders of magnitude faster than electron injection from the TiO_2. While the exact ratio would be dependent on the specific system, solid hole-conductors seem to disfavor carrier recombination more than a liquid electrolyte system. Early research to replace the liquid electrolyte explored replacing it with conductive, organic polymers[29,30]; more recently the use of inorganic semiconductors as possible alternatives has emerged[31,32].

2.2.3   *Quantum dot-sensitized solar cells*

Quantum dot-sensitized solar cells replace the dyes in dye-sensitized solar cells with quantum dots. To evaluate the properties that quantum dots exhibit which make them ideal for solar cells, returning to nature's photosynthetic system is necessary. Quantum dots closely mimic the reaction center in photosynthesis. To provide a visual comparison of charge generation and migration within quantum dot-sensitized solar cell and during photosynthesis, Figure 2.2 depicts a simplified version of a quantum dot-sensitized solar cell beside the P_{700} reaction center of photosystem I. The similarities of the two systems are readily apparent with a light-harvesting unit (chlorophyll or quantum dot) becoming excited by light to generate an electron-hole pair which is separated and each carrier is transferred through different media (either across a

thylakoid membrane or within nanoparticle network) along the energetic gradient of the charge-carriers. However, the electron-transfer rate in photosystem I is 47 e^-/s[33] which is minimal compared to the electron-transfer rate between quantum dots and TiO_2 which is reported to be between 10^7 and 10^{10} e^-/s depending on the binding environment of the quantum dots[34,35].
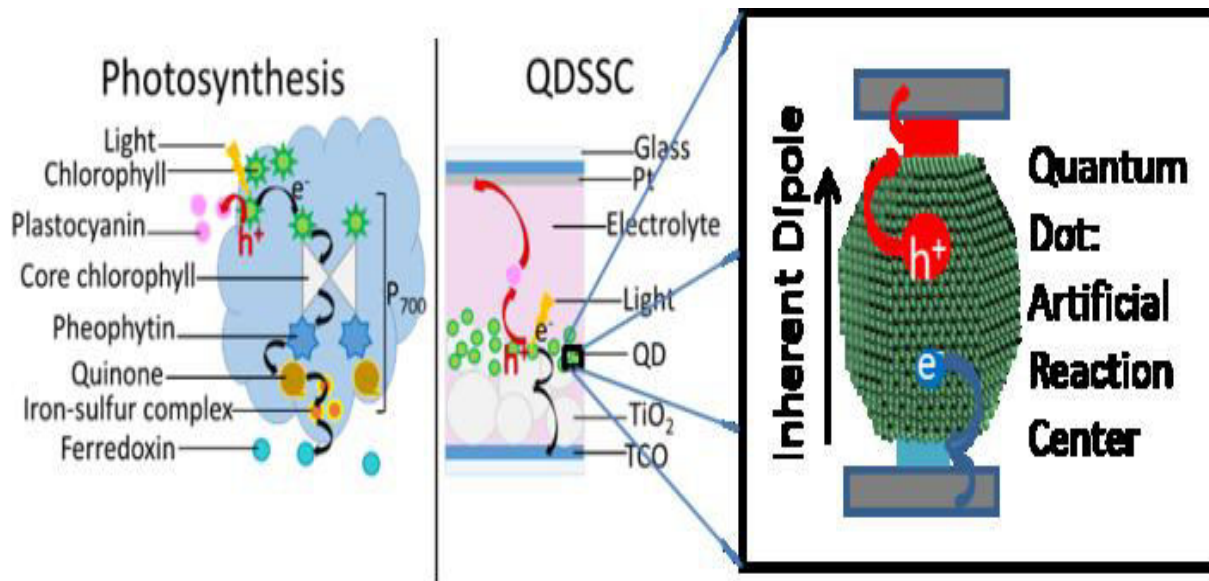
Figure 2.2 Comparison of charge generation and migration during photosynthesis in the P_{700} reaction center of photosystem I and during photoexcitiation in a quantum dot which acts as an artificial reaction center in a quantum dot-sensitized solar cell (QDSSC)

In addition to the above similarities of the entire quantum dot-sensitized solar cell to photosystem I, quantum dots act as an artificial reaction center, separating the electron and hole on the femtosecond timescale[36,37] with the carries moving along the energetic gradient created by the inherent dipole of the quantum dot[38] due to top and bottom terminating planes of cations or anions[39]. Similar to photosystem I, quantum dots rely on quantum mechanics and nanostructuring to optimize energy collection[40], leading to molar extinction coefficients several orders of magnitude higher than their dye-counterpoints with electronic and optical properties that are size-tunable. Also, quantum dots are inorganic particles which makes them more robust and less prone to photo-bleaching.

14

2.3 Overview

The rest of part 1 describes the design and fabrication of a nanostructured, solid-state solar cell. The studied devices incorporate TiO_2 nanotubes, PbS or CdSe quantum dots, and indium tin-oxide. In the studied nanostructured, solid-state device (Figure 2.3), quantum dots absorb photons, generating an electron-hole pair. The photo-generated electron, traveling down its energy gradient, is injected into a TiO_2 nanotube, where it travels out of the device into the Ti foil contact. The photo-generated hole, following a path similar to those discussed by Gao et al. for hole conduction in n-type metal oxides[41], transfers into indium tin oxide via shallow gap states. The device is analogous to dye-sensitized solar cells with the critical difference being that the device separates charge generation and migration by utilizing a unique combination of inorganic solid materials, which removes sealing and leakage issues associated with liquid electrolytes and should reduce carrier recombination.
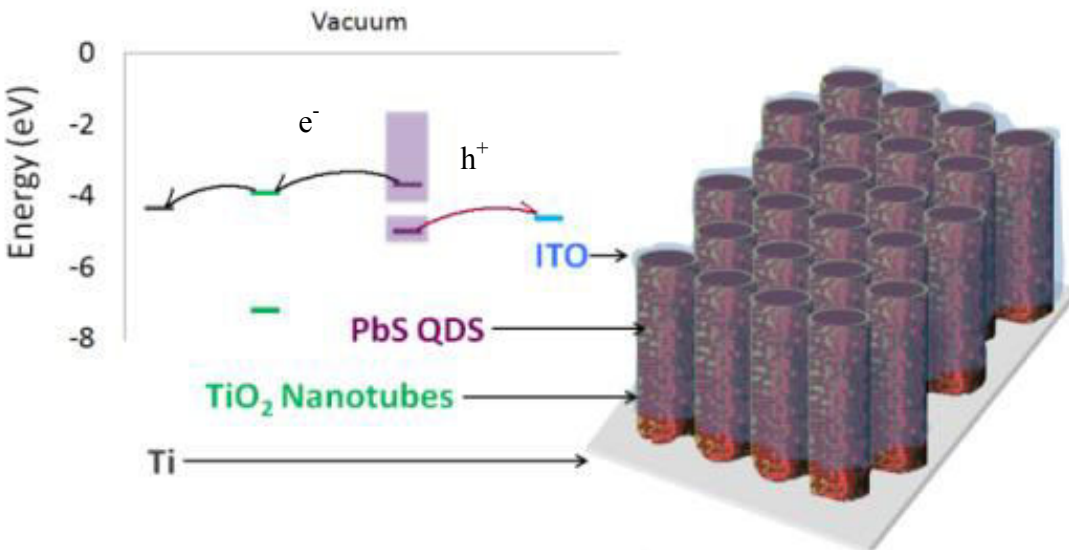
Figure 2.3 Nanostructured, solid-state photovoltaic device design: PbS quantum dots (QDs) form a layer at the interface between TiO_2 nanotubes and indium tin oxide (ITO). Upon excitation of the quantum dots, photoexcited electrons inject into nanotubes and the holes transfer into the indium tin oxide to be carried to an external circuit to perform work.

EXPERIMENTAL METHODS

3.1 Fabrication of Vertically Aligned TiO₂ Nanotube Array
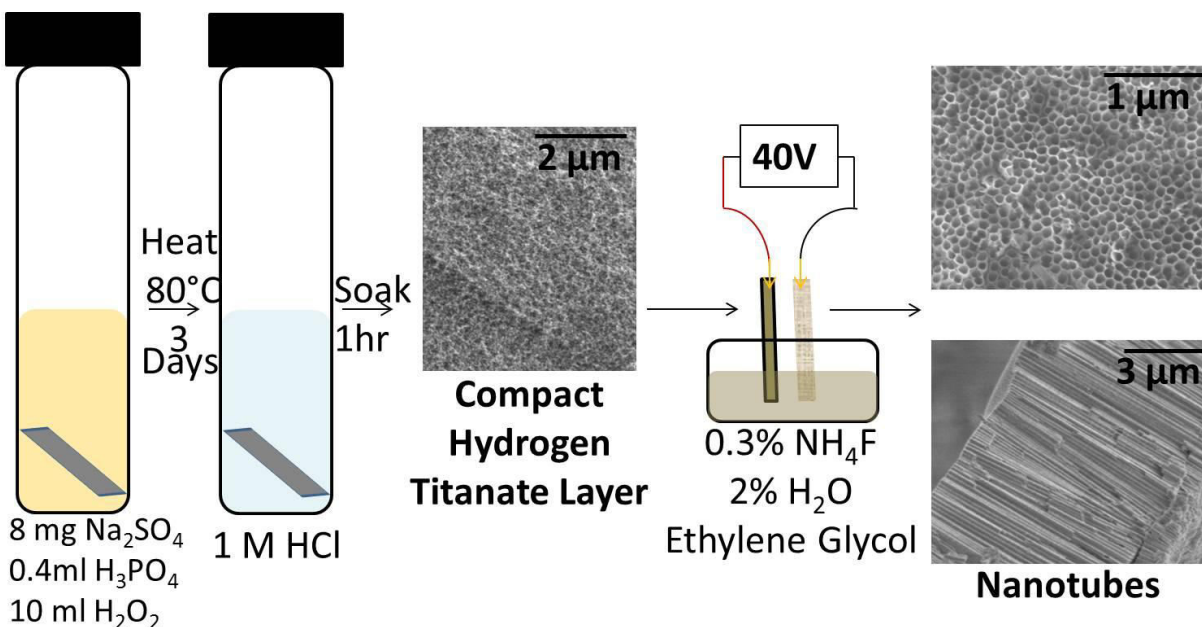
Figure 3.1 Schematic depicting the fabrication TiO₂ nanotubes from a Ti foil

3.1.1 Hydrogen peroxide pre-treatment

All chemicals unless otherwise noted were ACS-grade purchased from Sigma-Aldrich and were used without further modification. A Ti foil (0.25 mm thick, 97% purity, cut into 1" × 1" squares using a machine press) was cleaned by sonicating in isopropanol and acetone for 1 minute each. A hydrogen peroxide solution composed of 10 ml of hydrogen peroxide, 0.4 ml of H_3PO_4, and 8 mg of Na_2SO_4 was prepared. The clean foil was pretreated by soaking in the hydrogen peroxide solution at 80°C for three days.[42] During this time a compact layer of sodium-titanate was formed. Soaking the foil in 1M hydrochloric acid (EMD ACS-grade) for one

hour eliminates the sodium through a cation exchange with hydrogen forming hydrogen titanate. The foil was rinsed with deionized water and dried using nitrogen.

3.1.2 Anodic oxidation

After pretreatment, the foil was anodized at 40 V for two hours in a two-electrode electrochemical cell. During anodization, the foil was held parallel to a platinum mesh counter electrode at a distance of 0.5 cm, using a custom-built vertical stand. The electrodes were partially submerged in an ethylene glycol electrolyte containing 0.3% ammonium fluoride and 2% water. To prepare the electrolyte, 0.1440 g of ammonium fluoride was dissolved in 0.4 ml of deionized water and diluted to a final volume of 40 ml with ethylene glycol. A potential was applied and maintained between the two electrodes using a Keithley 2400 source meter interfaced with an Apple G3 computer running a custom LabView script. After anodization, the nanotube array was rinsed with ethanol, sonicated in ethanol for 30 seconds, and dried under nitrogen flow.

3.2 Synthesis of Colloidal Quantum Dots

3.2.1 Oleic acid-capped CdSe

CdSe quantum dots were synthesized as follows: 0.25g CdO, 1.5 ml oleic acid, and 18.5 ml octadecene are stirred and heated to 280°C in a sealed 3-neck flask under argon flow. A temperature probe and heating mantle were used to monitor and maintain appropriate heating conditions. To remove excess water, the reaction vessel was purged using a 12-guage needle inserted into a rubber septum until the reaction temperature reached 150°C. Once the reaction solution reached 280°C, the solution went clear indicating the brown CdO had converted to colorless Cd-oleate. The reaction was cooled to 150°C, and a solution of 0.5g trioctylphenylphosphine oxide, 1.5g octadecylamine, and 8ml octadecene heated to 80°C was

injected to aid in shape-control during quantum dot growth. The reaction solution was heated to 280°C, and 1ml 1.5M Se: tributylphosphine (2.37g Se powder dissolved in 20ml tributlyphosphine) was injected. The reaction solution quickly changes to a dark, reddish brown color indicating quantum dot production. The reaction vessel was cooled using compressed air to below 90°C. The resulting product was dispersed in toluene.

To remove excess ligands and remaining reactants, the product was washed using a series of precipitations and centrifugation. A small amount of the toluene-dispersed product was diluted with a large amount of ethanol and spun at 6500 rpm for fifteen minutes. The resulting pellet contained the desired quantum dots and was retained; the supernatant contains excess ligands and unreacted starting materials and was poured off the pellet and discarded. The pellet was dissolved in a small amount of toluene and a large amount of acetone was added. The solution was centrifuged at 6500 rpm for fifteen minutes. The supernatant was discarded and the clean pellet was diluted with hexanes.

3.2.2 Oleic acid-capped PbS

PbS quantum dots were synthesized as follows: 0.45 g PbO, 1.5 ml oleic acid, and 18.5 ml octadecene are stirred and heated to 150°C in a sealed 3-neck flask under vacuum in a fume hood. Once the solution went clear indicating Pb-oleate was produced, the flask reaction temperature was reduced to 120°C. In a separate 3-neck flask, 10 ml of octadecene was heated to 80°C under vacuum. A temperature probe and heating mantle were used to monitor and maintain appropriate heating conditions. In the nitrogen-atmosphere of a glove box, 0.290 ml hexamethyldisilathiane was drawn into a syringe. The syringe was capped and wrapped with Parafilm® for transfer from the glove box to the fume hood. Both reaction flasks were opened to argon gas flow to create a partially-positive pressure above the reaction solution. The

hexamethyldisilathiane was injected into the flask containing only octadecene. The entire

contents of the hexamethyldisilathiane flask were then pulled into a syringe and transferred to the

flask containing Pb-oleate. The reaction solution quickly changes to a black indicating quantum

dot production. The reaction vessel was cooled using compressed air to below 90°C. The

resulting product was diluted with acetone. To remove excess ligands and remaining reactants,

the product was washed using a series of precipitations and centrifugation. The product in

acetone was spun at 7500 rpm for fifteen minutes. The resulting pellet contained the desired

quantum dots and was retained; the supernatant contains excess ligands and unreacted starting

materials and was poured off the pellet and discarded. The pellet was dissolved in a small

amount of hexanes and a large amount of ethanol was added. The solution was centrifuged at

7500 rpm for fifteen minutes. The supernatant was discarded and the clean pellet was diluted

with hexanes.

3.3 Deposition of Quantum Dots

3.3.1 Electrophoretic deposition
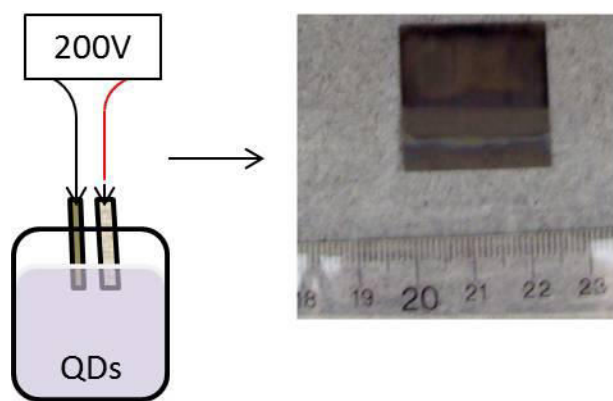
Figure 3.2 Schematic depicting the electrophoretic deposition of quantum dots (QDs) into TiO_2 nanotubes and a photo of the result

For electrophoretic deposition (EPD), the nanotube array and a platinum mesh counter

electrode (separation = 0.5 cm) were submerged in an optically dilute (O.D.= 0.05 a.u.) solution

of quantum dots in hexanes.[43] The array, anode, and mesh, cathode, were held parallel using a custom-built vertical set-up. A potential of 200 V was applied between the electrodes for twenty minutes. The potential was applied and maintained between the two electrodes using a Keithley 2400 source meter interfaced with an Apple G3 computer running a custom LabView script. The electric field between the electrodes induced quantum dot migration and adhesion to both of the electrodes. After deposition, the array was rinsed with hexanes to remove excess quantum dots.

3.3.2 Chemical-linking
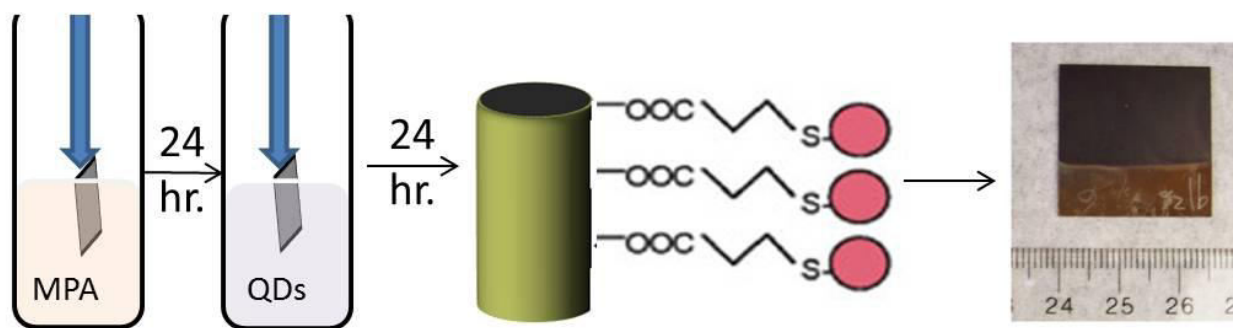
Figure 3.3 Schematic depicting chemical-linking of quantum dots (QDs) to TiO$_2$ nanotubes using 1,3-mercaptopropionic acid (MPA) and a photo of the result

Chemical-linking uses a bifunctional ligand (1,3-mercaptopropionic acid, in this case) to create a direct link between the surface of the nanotubes and the quantum dots.[44] The nanotube array was soaked in a 10% 1,3-mercaptopropionic acid in methanol solution for 24 hours; the soaking was carried out in a covered, glass Petri dish to prevent evaporation. The carboxylic acid group of ligand bound to the surface of the nanotubes during this time. The array was rinsed with methanol and transferred to an optically dilute (O.D. =0.05 a.u.) solution of quantum dots in hexanes, where it soaked another 24 hours. The thiol group on the ligand links to the quantum dots during this time. The array was rinsed with hexanes to remove excess quantum dots.

3.3.3 Successive ion layer adsorption and reaction
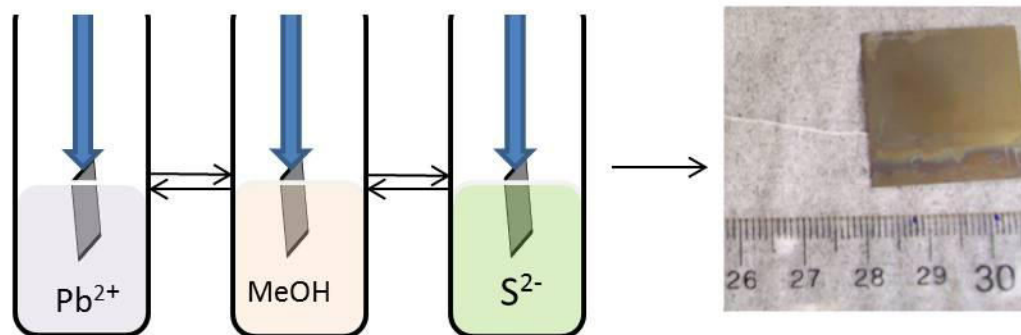
Figure 3.4 Schematic depicting successive ion layer adsorption and reaction to fabricate *in-situ* quantum dots in TiO$_2$ nanotubes and a photo of the result

Successive ion layer adsorption and reaction, commonly known as SILAR, is a relatively simple process that synthesizes the quantum dots directly onto the substrate of interest[45] rather than using pre-synthesized colloidal quantum dots. The nanotube array was soaked in 1mM lead acetate solution (38.8 mg in 100 ml methanol), rinsed with methanol, soaked in 1mM sodium sulfide (8.8 mg in 100 ml methanol), and rinsed again with methanol. Each step took one minute. Lead ions that adsorb to the surface of the nanotubes during the first step were reacted with sulfur ions in the third step to nucleate PbS quantum dots. The entire process is repeated for a total of five cycles to ensure quantum dot nucleation and growth.

3.4 Indium Tin Oxide Deposition

3.4.1 Electrochemically-assisted deposition

For electrochemically-assisted deposition, the nanotube array sensitized with quantum dots, a platinum mesh counter electrode, and a Ag/AgCl reference electrode are submerged in an 80°C solution of 10mM $In(NO_3)_3$, 1M KNO_3, 4.6mM HNO_3, and 1mM $SnCl_4$[46,47]. When an optimal reduction potential of -0.8V (determined by linear sweep voltammetry on Ti foil in 1M KNO_3) is applied, a localized pH increase generated by the reduction of nitrate and dissolved oxygen causes indium tin hydroxide complexes to precipitate out of solution into the nanotube array.

Since the reaction relies on the reduction of nitrate and dissolved oxygen, the optimal reduction potential was determined. A simplified solution consisting of 1M KNO_3, adjusted to pH of about 2.3 using 1 M HNO_3, was heated to 80°C using a water bath. A Ti foil, platinum counter electrode, and $Ag/AgCl_2$ reference electrode were partially submerged into the solution. CHI660A Electrochemical Workstation was utilized to perform linear sweep voltammetry, scanning potentials from 0 to -1.4 V at a rate of 0.1 V/S and monitoring the current at each step. The point where the current reaches a maximum, 0.8 V, was taken to be the optimal reduction potential.

To prepare the reaction solution, 0.40 g KNO_3, 0.13 g $In(NO_3)_3$, 0.014 g of $SnCl_4$, and 1.2 ml of 0.158 M HNO_3 (1 ml concentrated HNO_3 in 9 ml H_2O). The solution was heated in a water bath to 80°C.

The quantum dot-functionalized nanotube, platinum counter electrode, and $Ag/AgCl_2$ reference electrode were partially submerged into the reaction solution. CHI660A

Electrochemical Workstation was utilized to apply the optimal reduction potential for a specified amount of time. The potential is maintained by the software at -0.8 V for fifteen minutes.

Subsequent annealing converts the hydroxide complexes to indium tin oxide. A Lindberg-Blue HTF55000 Series Hinged Tube Furnace with quartz tube was used to anneal the samples. The samples were annealed for 3 hours at 450°C with heating and cooling ramp periods of 3 hours.

3.4.2 Electron beam evaporation

For electron beam evaporation an Ångstrom Åmod e-beam chamber (Ångstrom Engineering; Kitchener, ON) was utilized. The quantum dot-functionalized nanotubes were masked and attached to the loading plate of the e-beam using copper tape. The samples were suspended above an ITO target comprised of 90% indium oxide doped with 10% tin oxide. The target was evaporated using a steady state power of ~3.5% (~210 kW) to maintain a deposition rate of 0.5Å/s. The slow deposition rate and rotation of the substrate ensures that indium tin oxide penetrates the high aspect ratio nanotubes rather than occluding the nanotube apertures at the top of the array (i.e. "keyholing"). The deposition amount was a total planar thickness of 40 nm as reported by the system's quartz-crystal microbalance and confirmed by profilometry of a sample of indium tin oxide deposited on a glass slide.

Subsequent annealing crystallizes the deposited amorphous indium tin oxide. A Lindberg-Blue HTF55000 Series Hinged Tube Furnace with quartz tube was used to anneal the samples. The samples were annealed for 3 hours at 450°C with heating and cooling ramp periods of 3 hours.

3.5 Characterization Techniques

3.5.1 Glancing angle x-ray diffraction

X-ray diffraction probes the spacing of atomic planes within a crystal by observing the patterns of interference created by the reflection of x-ray waves by a sample. If the angle of incidence of an x-ray beam striking a surface is adjusted so that the wavelength of probe x-ray equals twice the interatomic spacing of a set of lattice planes, the reflected x-ray waves interact coherently to produce a strong signal; otherwise, the waves interact destructively and signal is minimal. Since the interatomic spacings of crystal planes of a material are unique, crystalline materials generate unique diffraction patterns, allowing identification of the material and its crystal structure by comparing within patterns of known samples. Assuming peak broadening is only due to size effects, the average grain size for materials can be calculated using Scherrer's equation.[48]

$$d = \frac{0.9\lambda}{\beta cos\theta} \qquad \text{Eqn (3.1)}$$

For a given peak, β is the full width half maximum in radians, θ is the Bragg angle, and λ is the wavelength of incident radiation (0.154056 nm for Cu Kα).

If the surface of the material is of more interest than the bulk, the x-ray probe can be fixed at a shallow incident angle so that the x-ray predominately interact with only the surface of the sample; a technique known as glancing angle x-ray diffraction. To obtain the angle of incidence with the lattice planes, the detector is rotated rather than the source.

Glancing angle x-ray diffraction patterns were obtained using a Scintag X1 θ/θ automated powder X-ray diffractometer with a Cu target (λ = 1.54056 Å), a Peltier-cooled solid state detector, and a zero-background Si(510) sample support, with an incident probe angle of 1°. Diffraction patterns were collected from devices after annealing.

3.5.2 Scanning electron microscopy and energy dispersive x-ray spectroscopy

Scanning electron microscopy creates images of a sample by collecting the secondary electrons inelastically scattered by a sample as a high-energy (20 kV) electron beam is rastered across the sample. Each pixel of the generated image is a grey-scale correlation of the intensity of the measured signal for a raster point on the sample.

High energy electrons, in addition to being scattered by a sample, also excite core-shell electrons of sample atoms to higher energy levels. When the hole created in the lower energy-level by the exiting electron is filled by a higher-energy electron relaxing into it, an x-ray with energy corresponding to the energy difference between the higher and lower energy levels is emitted. The energy of the emitted x-ray has a specific energy characteristic of the element of the atom that emitted the x-ray. By collecting and measuring the energy of x-rays emitted by a sample, the elemental composition of that sample; this technique is known as energy dispersive x-ray spectroscopy. If the electron beam is rastered across a sample and x-ray information is collected at each particular spot, the elemental composition of a sample can be spatially correlated with the sample image to generate elemental maps of the sample.

In the current work imaging of devices at various stages of completion were conducted using a Hitachi S-4200 scanning electron microscope equipped with a cold-field emission, tungsten filament source. Surface topography of devices at various stages of completion was evaluated using scanning electron microscopy. Samples were prepared from imaging by adhering the backside of the device's titanium foil to the stage using conductive carbon tape. It is important that the samples have an electrical contact with the stage to prevent sample charging. From images of bare nanotubes, the nanotube pore diameter, wall thickness, and interpore spacing were determined. From images of nanotubes functionalized with quantum dots,

occlusion of quantum dots onto of the nanotubes was assessed. Surface cracking was evaluated by imaging completed devices after annealing.

To evaluate the infiltration of quantum-dots and indium tin oxide into the nanotube arrays, energy dispersive x-ray spectroscopy was utilized to create elemental maps of side profiles of quantum dot-functionalized nanotubes and completed devices. In order to gain access to the side profiles, samples were broken and scrapped onto carbon tape.

3.5.3 Transmission electron microscopy

Transmission electron microscopy collects information about a sample from the density and energy of electrons transmitted through a thin film sample. A high energy (200 kV) electron beam is directed onto a thin film sample. Depending on the thickness, atomic composition, and crystallinity of the sample, the intensity and location of transmitted electrons varies. Thick samples and samples containing elements of high atomic numbers allow few electrons to pass, so the resulting image appears dark. Planes of atoms occuring in regular, repeating patterns, as in crystalline materials, diffract electrons creating interference patterns that appear as repeating dark lines in the image. These dark lines are referred to a lattice fringes and can be used to identify the crystalline material and evaluate its quality.

In the current work, a Philips CM 20 transmission electron microscope with a LaB_6 emission source operating at 200 kV was utilized. Quantum dot size, polydisperisty, and crystallinity was evaluated by imaging samples of quantum dots cast onto ultrathin lacey carbon films on copper grids. Optically-dilute solutions of quantum dots were dropcast onto the grids while the grid was held in anti-capillary tweezers. Excess solvent was wicked away using a Chem-Wipe®.

To evaluate infiltration of the quantum dots into the nanotubes, samples of quantum dot-functionalized nanotubes were broken and scrapped into isopropanol. To ensure the broken sections would be electronically transparent, the samples were sonicated for 10 minutes. The samples were cast in the same manner as the quantum dot samples.

3.5.4 Inductively-coupled plasma optical emission spectroscopy

Inductively-coupled plasma optical emission spectroscopy (ICP-OES) is used to determine the concentration of elements contained within a liquid sample. The working principle behind ICP-OES is that thermally-excited atoms emit characteristic wavelengths of light. By comparing the intensity of a characteristic wavelength of light generated by atoms in an sample of unknown concentration to that created by samples of known concentrations, the concentration of the unknown sample can be interpolated.

To evaluate the concentration of quantum dots deposited into nanotube arrays, samples were digested by a solution containing 0.3 ml HNO_3 and 4 ml hydrogen peroxide at 95°C. Digestion of the devices on the Ti foil, results in dark orange solutions due to the high concentration of Ti. To prevent clogging of the capillary tubes used to flow sample into the spectrometer, the sample solutions were diluted 100 fold by mixing 1 ml of the sample solution with 99 ml of deionized water. Elemental content of acid-digested samples was determined using a Perkin-Elmer Optima 7000 DV inductively-coupled plasma optic emission spectrometer. The working parameters used during measurements were as follows:

Plasma Gas Flow: 15 L/min
Auxiliary Gas Flow: 0.2 L/min
Nebulizer Gas Flow: 0.8 L/min
Pump Flow Rate: 1.50 mL/min
Radio Frequency (RF) Power: 1300 W

To calibrate the instrument, standards with known concentration of the elements of interest were prepared and measured prior to measuring the samples. To prepare the known standards, 5 ml of 10µg/ml multi-element calibration standard (purchased from Perkin-Elmer) was pipetted using a calibrated mirco-pipette into a 50 ml volumetric flask. The flask was filled to the mark with Millipore water, creating a 1 µg/ml standard solution.

The reported concentration of elemental lead was used to determine the areal density of quantum dots in the nanotube array. To calculate the areal density, the concentration reported in µg/ml was converted to mass of lead by multiplying the reported concentration by the volume of prepared sample solution. Assuming that PbS quantum dot-density is equal to that of PbS bulk (7.16 g/cm^3), the volume of lead contained in the device was determined. To determine number of quantum dots, the volume of lead was divided by the volume occupied by a single PbS quantum dot. For this calculation, it was assumed the quantum dots were perfect spheres of average diameter of 3.9 nm. The areal density of quantum dots within the nanotube array was determined by dividing the number of quantum dots by the area of the nanotube array, measured prior to digesting the sample.

3.5.5 Surface wettability

Surface wettability describes how readily a fluid will spread to coat a surface and is dependent upon the free energy of the surface and the surface geometry. Anything that alters these parameters may cause variations in the surface wettability.[49] For example, increasing the polar nature of the chemical composition of a surface increases the free energy of the surface in contact with water, resulting in a lower contact angle.[50] Increasing the surface area of a surface effectively increases the free energy of a surface, which would thus seemingly lower the contacting angle; however, the impact of increased surface area is a bit more complex and is

dependent upon the nature of the surface.[51] Wenzel's law indicates that increasing the surface area of a hydrophilic surface does lower the contacting angle but increasing the surface area of hydrophobic surface increases the contact angle. The introduction of trapped air between the surface structures and the water droplet also increases the contacting angle.

Contact angles were measured with a Rame-Hart goniometer on static 5 μL drops of deionized water. A syringe was used to apply deionized water onto the surface of the samples, during which the needle of the syringe remained inside the droplet as the contact angle measurements was measured. Contact angles were measured to determine the hydrophobicity of bare nanotubes and nanotubes functionalized with quantum dots.

3.5.6 Photovoltaic response

For photovoltaic response testing, the devices were illuminated with broadband, white light from a tungsten filament lamp (50W Solux 4700K lamp). The set-up was calibrated using a Coherent Radiation Model 210 power meter so that at the desired testing distance the tested device received a power input of $1000W/m^2$. The device was connected to a Keithley 2400 source meter, controlled by a voltage sweep LabView program written by Dr. Nathanael Smith. The voltage was swept from 0 to 0.5V with a step interval of 0.01V. Measurements were taken of devices in the dark and under illumination.

CHAPTER IV

SOLID-STATE QUNATUM DOT-SENSITIZED SOLAR CELL

4.1 Introduction

Development of novel all-solid-state, all inorganic photovoltaic devices requires a unique combination of fabrication and characterization techniques. The research presented here analyzes photovoltaic response and material characterization to determine the impact that deposition technique has on the infiltration, quality, and performance of light harvesters and hole extraction materials in a nanostructured, solid-state device. The studied devices utilize inorganic oxides (titanium dioxide nanotubes and indium tin oxide (ITO)) as separate charge-transfer media for the extraction of electrons and holes generated by the photo-excitation of lead sulfide quantum dots. Quantum dots were deposited using three techniques successive ion layer adsorption and reaction, electrophoretic deposition, and chemical-linking. Deposition of ITO occurred via electron beam evaporation or electrochemically-assisted deposition. Infiltration of the quantum dots and ITO into the nanotubes was investigated using scanning electron microscopy with energy-dispersive x-ray spectroscopy. Morphology of deposited quantum dots was analyzed using transmission electron microscopy. Inductively-coupled plasma optical emission spectroscopy performed on acid digested devices was used to discern quantum dot loading. Simulated solar illumination and current-voltage measurements show that highest power densities (10^{-2} W/m^2) were generated by devices containing chemically-linked PbS quantum dots and electron beam deposited ITO.

4.2 Results and Discussion

4.2.1 Hydrogen peroxide pre-treatment of Ti foil

The pretreated foil when anodized yields nanotube arrays with wider pores (inner diameter increases by 37 nm) and less surface debris than untreated foils. The wider pores although slightly reducing the specific surface area of the nanotube array do allow easier infiltration of quantum dots and indium tin oxide. For visual comparison, scanning electron microscope images of planar and side views of nanotubes fabricated with and without pre-treatment are displayed in Figure 4.1
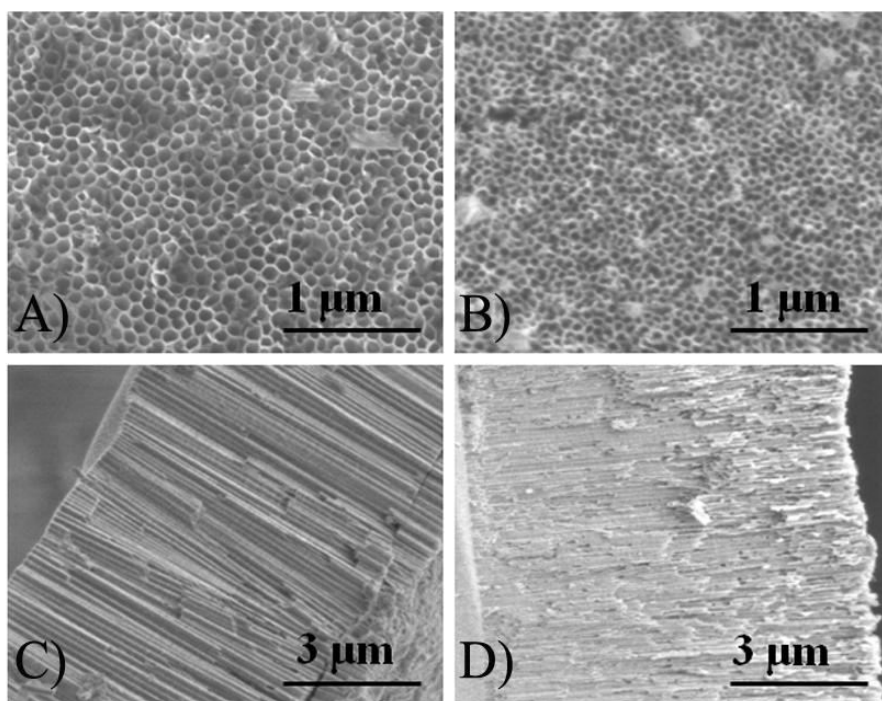
Figure 4.1 Scanning electron microscopy images of hydrogen peroxide pre-treated nanotubes top (A) and side (C) and untreated nanotubes top (B) and side (D)

4.2.2 Quantum dot infiltration and quality

The absorbance spectra of pre-synthesized colloidal PbS quantum dots and successive ion layer adsorption and reaction synthesized quantum dots on nanotubes, grown on a transparent conductive oxide on glass to allow transmittance of the light, are shown in Figure 4.2. For the pre-synthesized colloidal quantum dots used for electrophoretic deposition and chemical-linking, a single narrow absorption peak is observed at λ_{max}= 1170 nm. For the successive ion layer adsorption and reaction synthesized quantum dots the broadness of the peak at λ_{max1}= 1162 nm is indicative of the polydispersity that is further confirmed by transmission electron microscopy.

Transmission electron microscopy analysis (Figure 4.3) was used to determine the size of pre-synthesized quantum dots as 3.96 ± 0.03 nm and sizes for successive ion layer adsorption and reaction synthesized quantum dots as two prominent sizes 2.4 ± 0.6 nm and 4.3 ± 0.3 nm. In addition to size information, the transmission electron microscopy images of quantum dot-functionalized nanotubes shown in Figure 4.3 also indicate the non-spherical shape of successive ion layer adsorption and reaction quantum dots and possible agglomeration of the chemically-linked quantum dots.
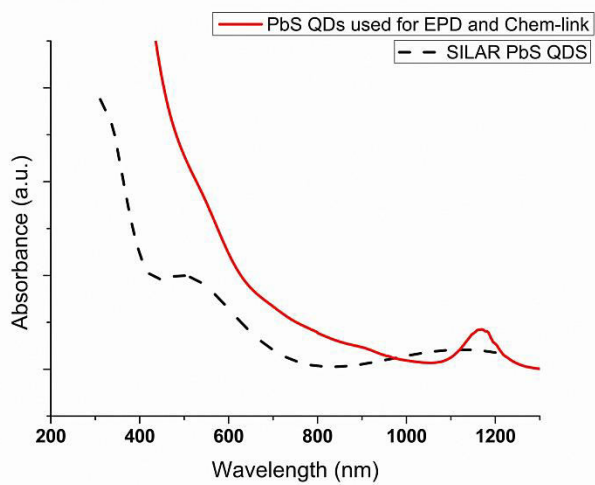
Figure 4.2 Optical absorption measurements of PbS quantum dots deposited using successive ion layer adsorption and reaction (SILAR), electrophoretic deposition (EPD), or chemical-linking
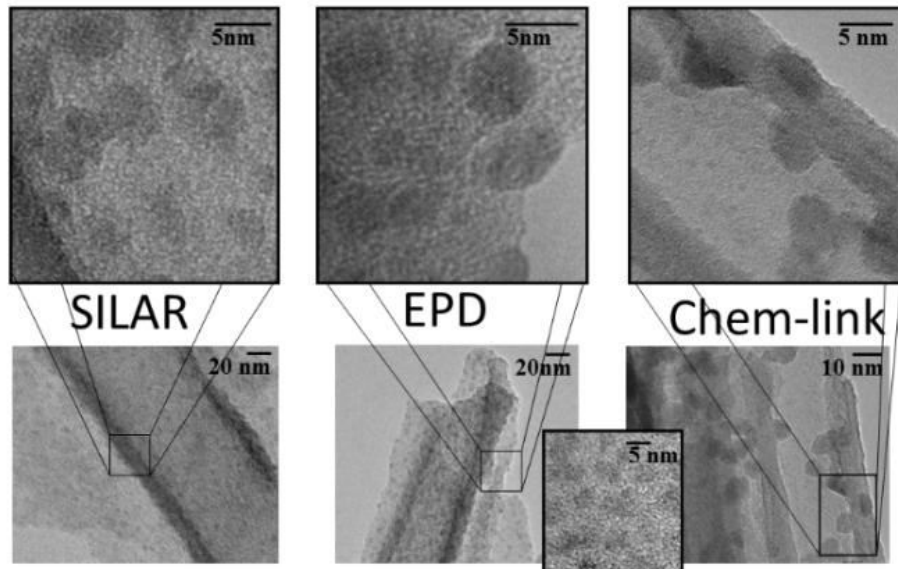
Figure 4.3 Transmission electron microscopy images of amorphous TiO$_2$ nanotubes with PbS quantum dots PbS quantum dots deposited using successive ion layer adsorption and reaction (SILAR), electrophoretic deposition (EPD), or chemical-linking (Chem-link) (Inset: pre-synthesized PbS quantum dots prior to their use in these techniques)

Glancing angle x-ray diffraction patterns (Figure 4.4) of amorphous (unannealed) nanotubes functionalized with quantum dots display broad peaks, typical of nanocrystals, that correspond to the JCPDS card 05-0592 for cubic PbS. The broadness of the peaks is due to the extremely small size and therefore limited long-range order of the lattice structure within quantum dots. The prominence of the peak associated with the (200) crystal plane in the successive ion layer adsorption and reaction quantum dot-containing device demonstrates a preferential growth along this axis during the growth process of the quantum dots. The preferential growth along this axis also explains the non-spherical shapes observed in the transmission electron microscopy images. The same lattice plane preference is not observed in the electrophoretic deposition and chemical-linking devices, which contain colloidal quantum dots.

33
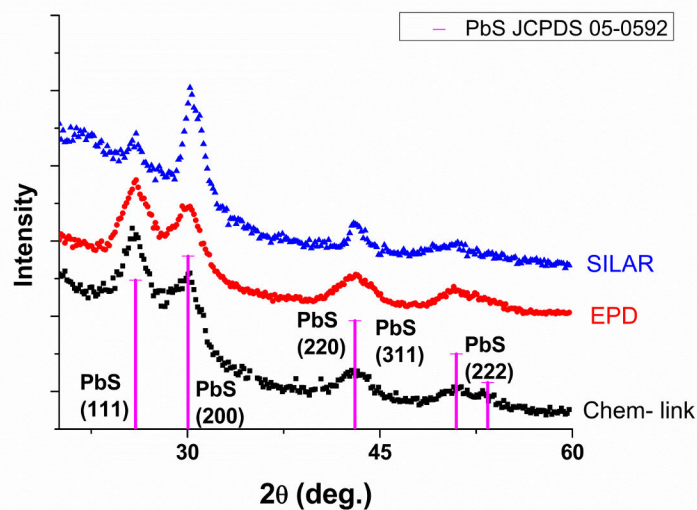
Figure 4.4 Glancing angle x-ray diffraction patterns of amorphous TiO_2 nanotubes with PbS quantum dots deposited using successive ion layer adsorption and reaction (SILAR), electrophoretic deposition (EPD), or chemical-linking (Chem-link)

A difficulty associated with working with nanotubes fabricated on a Ti substrate when depositing quantum dots from solution is overcoming surface-tension effects, which tend to inhibit the solution from completely filling the pores. Plan-view scanning electron microscope images of quantum dot-functionalized TiO_2 nanotubes shown in Figure 4.5 indicate quantum dots deposited using electrophoretic deposition and chemical-linking are partially occluded to the tops of the nanotube apertures. To assess infiltration of the quantum dots into the nanotubes, scanning electron microscopy coupled with energy dispersive x-ray spectroscopy of side-profiles were obtained. As observable in Figure 4.6, all profiles exhibit Pb and S signals along the length of the nanotubes, indicating infiltration of the quantum dots.

Colloidal quantum dots are surrounded by surface-passivating, hydrophobic ligands; the presence of these ligands may limit the infiltration of the aqueous solution used during EAD of ITO. To determine the hydrophobicity of nanotubes functionalized with quantum dots, the static contact angle of a drop of water on the surface of nanotube arrays was observed. The results

shown in Figure 4.7 indicate that bare nanotubes and nanotubes functionalized with quantum

dots synthesized using successive ion layer adsorption and reaction are hydrophilic having

contact angles <50°. Nanotubes functionalized with the pre-synthesized, colloidal quantum dots

are hydrophobic with contact angles >90°.
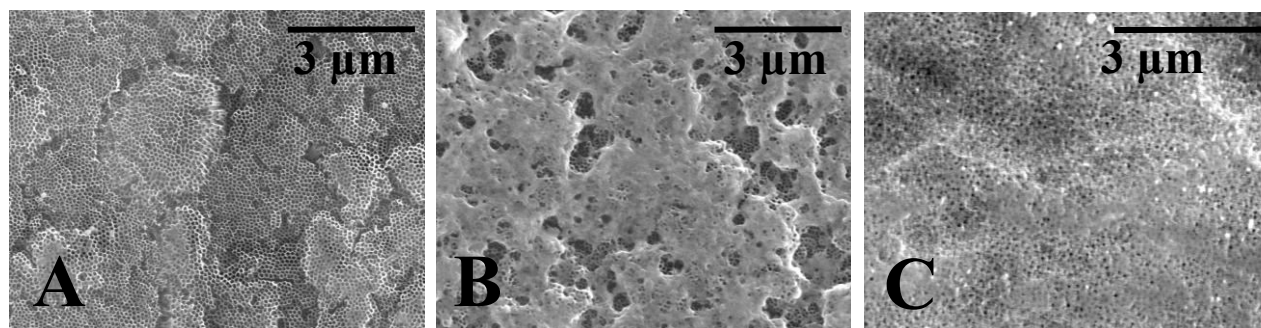
Figure 4.5 Plan-view SEM images of nanotube arrays sensitized with SILAR (A), EPD (B), or chemically-linked (C) PbS quantum dots
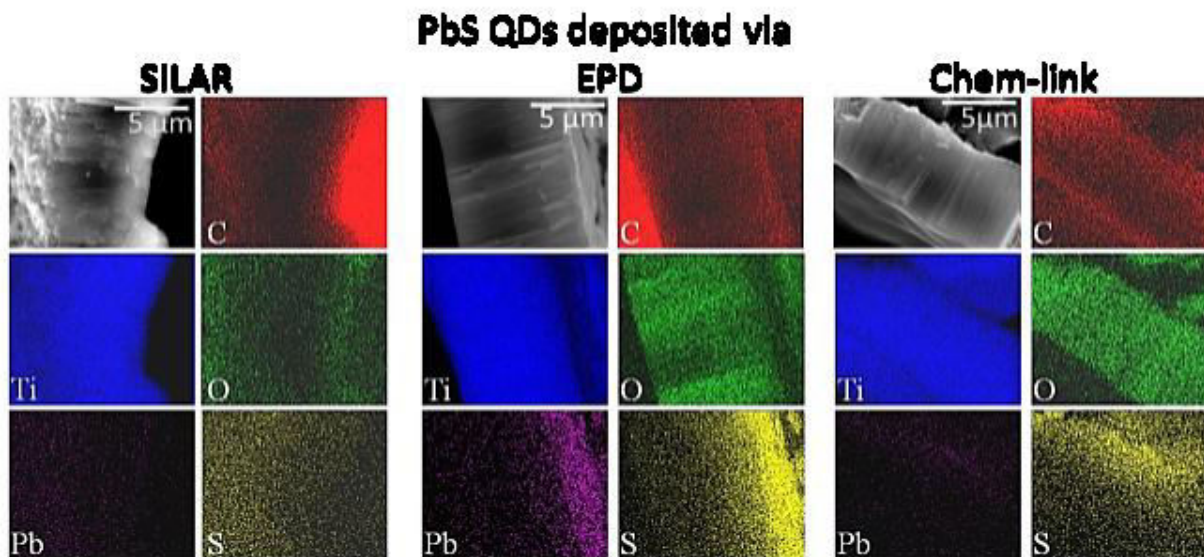
Figure 4.6 (Scale bar: 5 µm) Scanning electron microscopy-energy dispersive x-ray spectroscopy micrograph and elemental maps of side profiles of TiO$_2$ nanotubes with PbS quantum dots deposited using successive ion layer adsorption and reaction (SILAR), electrophoretic deposition (EPD), or chemical-linking (Chem-link)
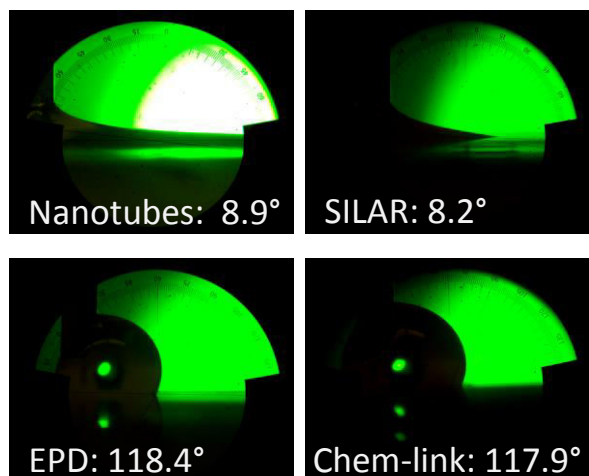
Figure 4.7 Images of advancing contact angle measurements (with the average of triplicate measurements shown in the inset) of water drops on the surface of bare nanotubes and of nanotubes sensitized with SILAR, EPD, or chemically-linked PbS quantum dots.

4.2.3 Indium tin oxide infiltration and quality

Given the importance of the electrical conductivity and optical transparency of the indium tin oxide in our devices, several figures of merit relating to these values were characterized. The resistivity was determined using a two-point probe system and a Keithley source meter controlled by a custom LabView voltage-sweep program.
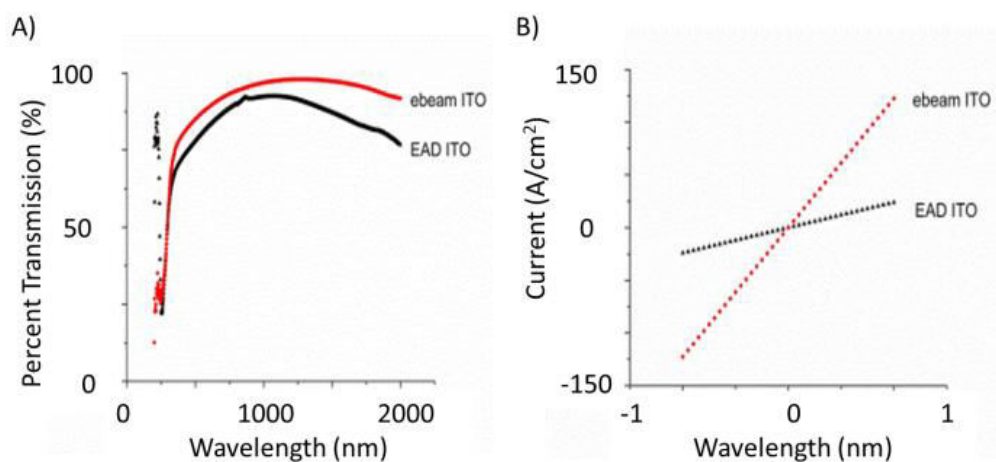
Figure 4.8 Percent transmission (A) and IV curves (B) of thin films of annealed indium tin oxide deposited on glass slides using either electrochemically-assisted deposition (EAD) or electron beam evaporation (ebeam)

In Figure 4.8A, current density vs. voltage for indium tin oxide deposited using both electrochemical assistance and electron beam evaporation are displayed. For the indium tin oxide deposited via electron beam evaporation, the resistivity is 0.0061 ± 0.0006 Ω-cm, which is comparable to other reported values of indium tin oxide annealed in air[47,52]. For the indium tin oxide deposited via electrochemical assistance, the resistivity is much higher at 0.0142 ± 0.0003 Ω-cm. The much higher resistivity may lead to limited hole extraction, making indium tin oxide deposited via electrochemical assistance a less ideal hole extraction material. As is observable in Figure 4.8B, indium tin oxide deposited by both techniques is between 70 to 90% transparent throughout nearly the entire solar spectrum, so in terms of light transparency both deposition methods produce indium tin oxide that is well-suited for use as front-contacts in photovoltaic devices.

Utilizing the glancing angle x-ray diffraction patterns of annealed devices shown in Figure 4.9, the presence of anatase TiO_2 and In_2O_3 was confirmed. Since tin is substitutionally incorporated into the lattice of indium tin oxide, the diffraction peaks for tin oxide were not expected nor observed in the patterns collected[46,47]. Assuming peak broadening is only due to grain size effects, the average grain sizes are calculated using Scherrer's equation[48]. For the indium tin oxide-related In_2O_3 grains, the sizes are 19 nm for indium tin oxide deposited via electron beam evaporation and 22nm for indium tin oxide deposited via electrochemical assistance. The grain sizes for the indium tin oxide deposited by either method are similar and are small compared to the nanotube length (6 μm). Smaller grain sizes indicate more grain boundaries, which act as charge trap sites preventing effective transport through the material.
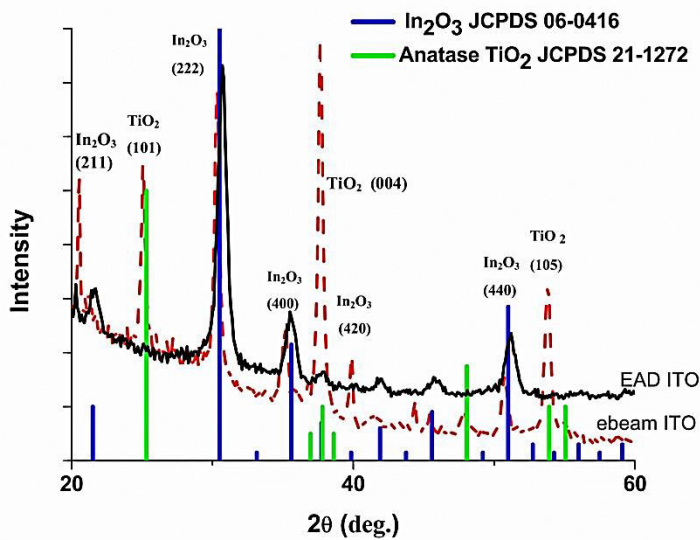
Figure 4.9 Glancing angle x-ray diffraction patterns of photovoltaic devices containing annealed TiO$_2$ nanotubes, PbS quantum dots, and indium tin oxide deposited using either electrochemically-assisted deposition (EAD) or electron beam evaporation (ebeam)

To evaluate the surface topography of the indium tin oxide, plan-view scanning electron microscope images of annealed devices were obtained. The topography of the device containing indium tin oxide deposited using electron beam evaporation shown in Figure 4.10 was much more uniform than that observed for the device containing indium tin oxide deposited with electrochemical assistance shown in Figure 4.11. The stark difference in the quality of the films generated by the different ITO techniques was readily observable. Cracking and particle-to-particle percolation increase charge trapping within photovoltaic devices.
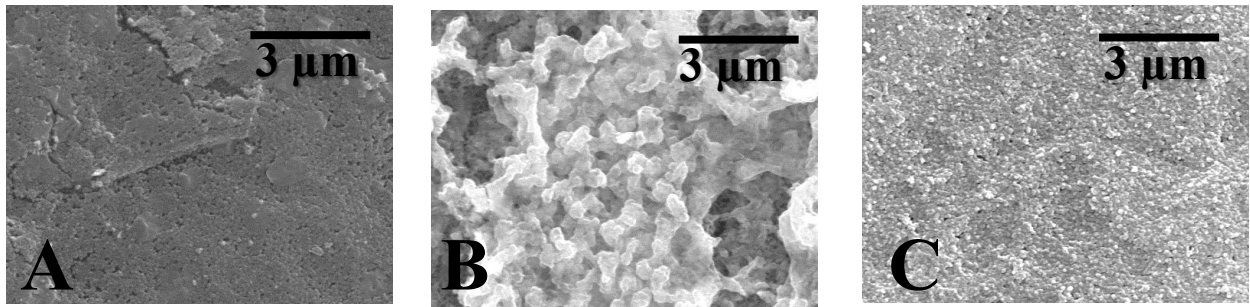
Figure 4.10 Plan-view SEM images of devices containing ebeam ITO and either SILAR(A), EPD (B) , or chemically-linked (C) PbS quantum dots
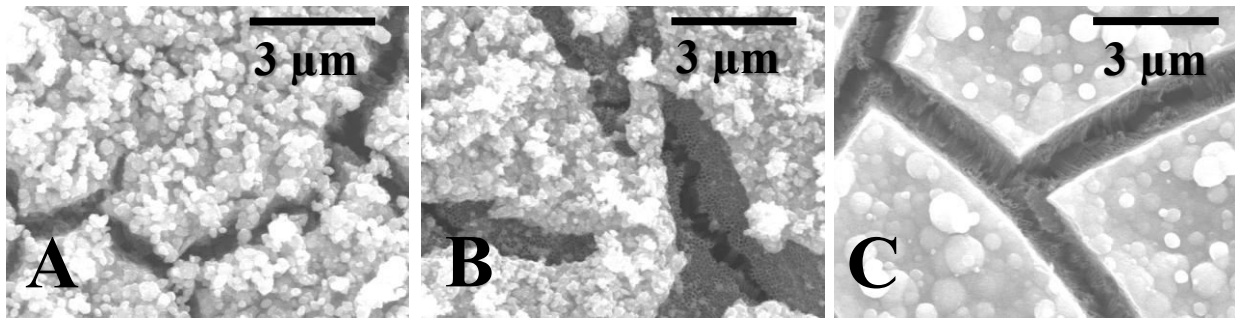
Figure 4.11 Plan-view SEM images of annealed devices containing EAD ITO and either SILAR (A), EPD (B), or chemically-linked (C) PbS quantum dots

4.2.4 Performance analysis of solar cells with indium tin oxide deposited via electrochemical

assistance

ITO Dep. Method	QD Dep. Method	Jsc (mA/cm2)	Voc (V)	FF	η
EAD	SILAR	$(-1.6 \pm 0.7) \times 10^{-6}$	$(5.0 \pm 0.1) \times 10^{-3}$	N/C	0
EAD	EPD	$(-1.8 \pm 0.8) \times 10^{-6}$	$(5.0 \pm 0.1) \times 10^{-3}$	N/C	0
EAD	Chem-link	$(-3.4 \pm 0.6) \times 10^{-4}$	0.07 ± 0.03	0.18 ± 0.01	$(6 \pm 2) \times 10^{-6}$
ebeam	SILAR	-0.004 ± 0.002	0.05 ± 0.01	0.21 ± 0.08	$(2 \pm 1) \times 10^{-5}$
ebeam	EPD	-0.005 ± 0.002	0.2 ± 0.1	0.16 ± 0.08	$(3 \pm 1) \times 10^{-5}$
ebeam	Chem-link	-0.05 ± 0.03	0.40 ± 0.01	0.16 ± 0.06	$(3.3 \pm 0.5) \times 10^{-3}$

Table 4.1 Summary of photovoltaic figures of merit, namely short-circuit current density (Jsc), open-circuit potential (Voc), fill factor (FF), and efficiency (η), for devices containing TiO_2 nanotubes infiltrated with PbS quantum dots and indium tin oxide through various deposition techniques.

As seen in Table 4.1 and Figure 4.12, the photovoltaic performance of devices containing indium tin oxide deposited via electrochemical assistance is minimal with the only device displaying a photoresponse being the one containing chemically-linked quantum dots.
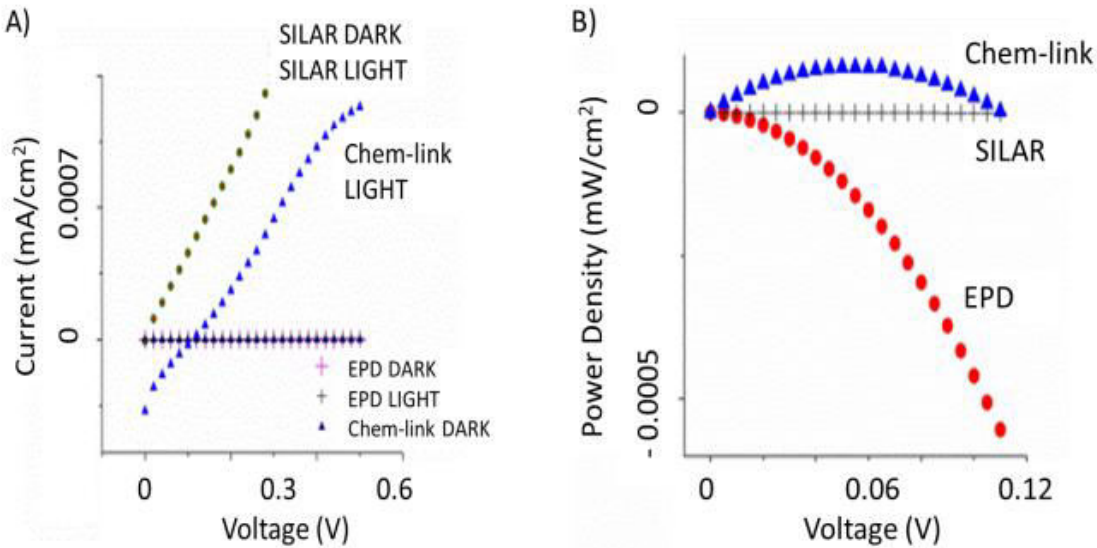
Figure 4.12 Typical current density (A) and power density (B) responses from nine replicates of photovoltaic devices containing TiO$_2$ nanotubes, indium tin oxide deposited via electrochemical assistance and PbS quantum dots deposited using successive ion layer adsorption and reaction (SILAR), electrophoretic deposition (EPD), or chemical-linking (chem-link).

A possible cause for poor device performance is the diminished active area due to limited infiltration of either the quantum dots or indium tin oxide deposited via electrochemical assistance. To investigate this possibility, scanning electron microscopy and energy-dispersive x-ray spectroscopy were used to analyze side profiles of the devices (Figure 4.13). The results of the scanning electron microscopy-energy dispersive x-ray spectroscopy elemental mapping of devices reveals that the lack of photo-response in the successive ion layer adsorption and reaction and electrophoretic deposition quantum dot devices arise from two different causes: dissolution of the quantum dots in the case of successive ion layer adsorption and reaction devices and the generation of a separated layer of indium tin oxide on top of the electrophoretic deposition quantum dot-device.

41
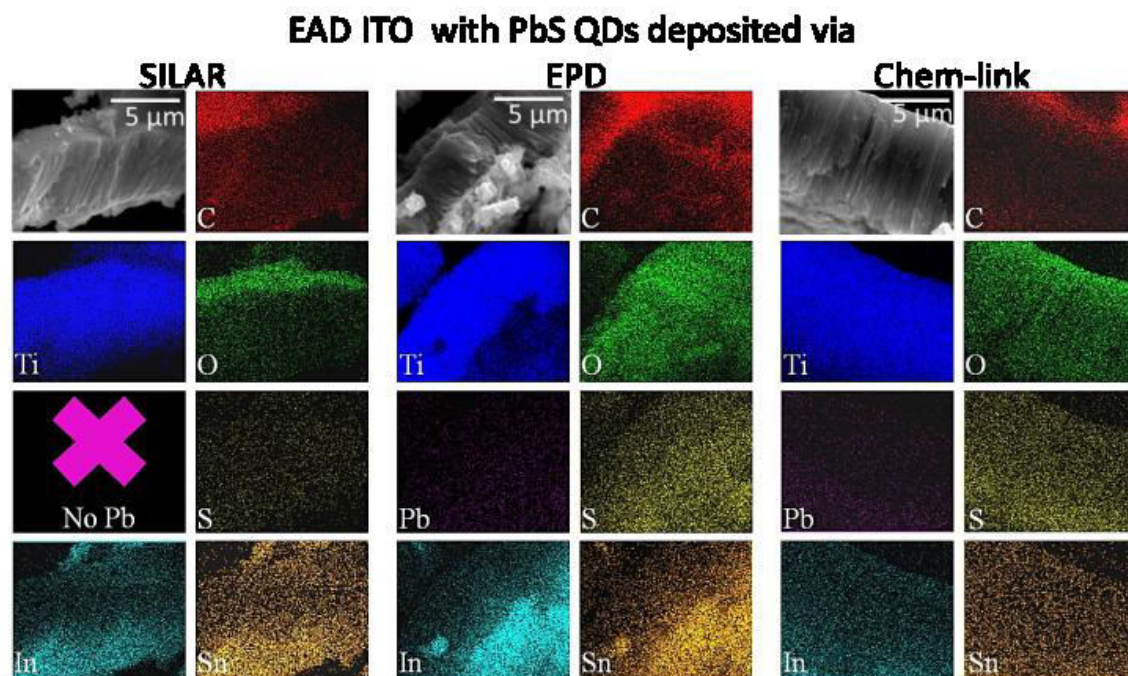
Figure 4.13 (Scale bar: 5 µm) Scanning electron microscopy-energy dispersive x-ray spectroscopy micrograph and elemental maps of side-profiles of photovoltaic devices containing indium tin oxide deposited via electrochemical assistance (EAD) and PbS quantum dots deposited using either successive ion layer adsorption and reaction (SILAR), electrophoretic deposition (EPD), or chemical-linking (Chem-link)

The device containing the successive ion layer adsorption and reaction quantum dots, shown in Figure 4.13, does not display a Pb signal within the device. Since prior to electrochemically-assisted deposition of indium tin oxide, a Pb signal is observed for all the quantum dot deposition techniques including successive ion layer adsorption and reaction (Figure 4.6), the probable cause for the signal loss is dissolution of the successive ion layer adsorption and reaction synthesized quantum dots, which unlike those deposited by electrophoretic deposition and chemical-linking, are not protected by surface ligands. The following reaction scheme is proposed for the dissolution of successive ion layer adsorption and reaction synthesized quantum dots, resulting in the observed scanning electron microscopy-energy dispersive x-ray spectroscopy maps which demonstrate no Pb-signal but definite S-signal.

42

$PbS_{(s)} \leftrightarrow Pb^{2+}_{(aq)} + S^{2-}_{(aq)}$ (Rxn 4.1)

$S^{2-}_{(aq)} + H_2O_{(l)} \leftrightarrow HS^{-}_{(aq)} + OH^{-}_{(aq)}$ (Rxn 4.2)

$H_3O^{+}_{(aq)} + S^{2-}_{(aq)} \leftrightarrow HS^{-}_{(aq)} + H_2O_{(l)}$ (Rxn 4.3)

$HS^{-}_{(aq)} + TiOH_{(s)} \leftrightarrow TiOH\text{-}SH_{(s)}$ (Rxn 4.4)
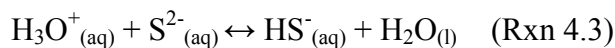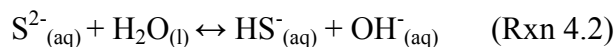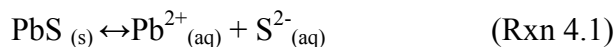
While typically only trace amounts of PbS (Ksp= 8×10^{-28}) dissolve in water, two natural side reactions occur to shift the equilibrium to favor dissolution. First, the sulfide anion, the conjugate base of a weak acid, is consumed in a hydrolysis reaction. Second, at the low pH conditions of electrochemically-assisted deposition, initially below 2.3, the solubility of PbS is increased even more by another side reaction, protonation of the sulfide anion[53]. Favoring PbS dissolution by reducing the concentration of dissolved S^{2-} occurs through any combination of reactions 2 and 3, and accounts for the disappearance of the Pb signal. The remaining S signal can be accounted for either by simple re-adsorption of S^{2-} or HS^{-} to the nanotubes or by the final step in the proposed process, which is the reaction of S with surface hydroxide groups, commonly found on unannealed nanotubes, to form titanium hydroxy-sulfide complexes[54,55].

The lack of a quantum dot layer between the oxides may cause the devices to short-circuit and generate the linear-type current response seen in Figure 4.12. In addition to scanning electron microscopy-energy dispersive x-ray spectroscopy data, calculation of the quantum dot concentration density pre- and post- indium tin oxide deposition using inductively-coupled plasma optical emission spectroscopy (ICP-OES) indicates a reduction in the density of successive ion layer adsorption and reaction quantum dots after electrochemically-assisted deposition. Figure 4.14 contains the comparative analysis of quantum dot-density of devices pre- and post- indium tin oxide deposition determined using observed Pb concentrations obtained

using ICP-OES of devices digested using a 2% nitric acid and 4% hydrogen peroxide solution.

The quantum dot concentration density for devices prior to indium tin oxide deposition are all

equal (within uncertainties), indicating the deposition technique utilized to deposit the quantum

dots did not impact the amount of quantum dots deposited within the nanotubes in this case.
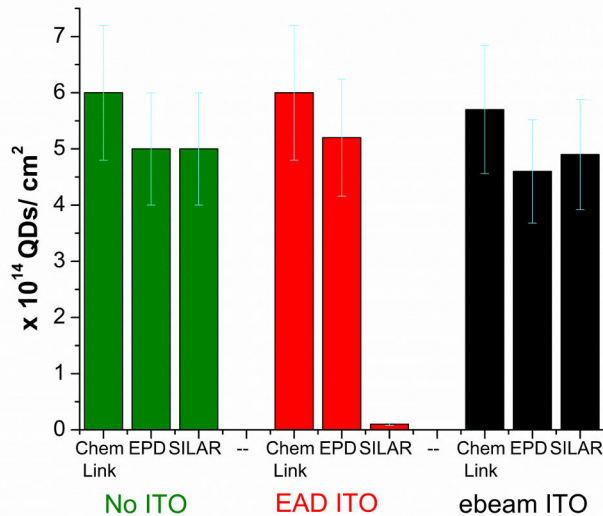
Figure 4.14 Quantum dot areal density for devices containing TiO_2 nanotubes, PbS quantum dots deposited using successive ion layer adsorption and reaction (SILAR), electrophoretic deposition (EPD), or chemical-linking (Chem-link), and either no indium tin oxide or indium tin oxide deposited using electrochemically-assisted deposition (EAD) or electron beam evaporation (ebeam). Quantum dot concentration based on Pb content obtained from acid-digested devices using ICP-OES and assuming PbS quantum dot density is equal to the PbS bulk density of 7.16 g/cm^3.

However, the concentration of the quantum dots after indium tin oxide deposited via

electrochemical assistance deposition does vary, especially for the successive ion layer

adsorption and reaction quantum dots. The concentration of successive ion layer adsorption and

reaction quantum dots decreased by over an order of magnitude after indium tin oxide

electrochemically-assisted deposition, confirming that dissolution of the unprotected quantum

dots occurred at a higher rate than that of the protected quantum dots.

Unlike the successive ion layer adsorption and reaction quantum dot device, the devices containing quantum dots deposited using electrophoretic deposition and chemically linked quantum dots, still display a uniformly distributed Pb-signal along the length of the nanotube array in scanning electron microscopy-energy dispersive x-ray spectroscopy elemental map and the same concentration of quantum dots before and after indium tin oxide deposited via electrochemical assistance deposition. The cause of the poor photo-response for the electrophoretic deposition device is a lack of infiltration of the indium tin oxide. The In-signal in the scanning electron microscopy-energy dispersive x-ray spectroscopy maps (Figure 4.13) while extending throughout the device show a large collection of In-containing material covering the top of the device but not interfacing within the nanotubes. Colloidal PbS quantum dots are surrounded by surface-passivating, hydrophobic ligands; the presence of these ligands may limit the infiltration of the aqueous solution used during electrochemically-assisted deposition of indium tin oxide.

To determine the hydrophobicity of nanotubes functionalized with PbS quantum dots, the advancing contact angle of a drop of water on the surface of nanotube arrays functionalized with quantum dots was observed. The results shown in Figure 4.7 indicate that the array functionalized with quantum dots deposited using electrophoretic deposition has the highest contact angle at slightly greater than 118°. However, the array with the chemically-linked quantum dots also has a comparably high contact angle, which since only a partial exchange of the surface ligands occurs during chemical-linking, is to be expected. It does indicate that the cause of the exclusion of the indium tin oxide in the electrophoretic deposition device is more complex than hydrophobicity issues alone.

Plan-view scanning electron microscopy micrographs of nanotubes functionalized with quantum dots are shown in Figure 4.5 and reveal the main reason for the exclusion of indium tin oxide from the TiO_2 pores in the electrophoretic deposition device. The nanotubes are almost completely sealed by quantum dots at the tops of the nanotubes. The separation of the indium tin oxide from the rest of the photovoltaic device causes a break in the circuit and results in the minimal current observed for the electrophoretic deposition devices seen in Figure 4.12.

While the devices containing chemically-linked quantum dots and indium tin oxide electrochemically-assisted deposition exhibit a photovoltaic response (Figure 4.12), the power generated is very small. One possible cause for the poor performance is revealed upon analysis of the topography of the indium tin oxide. Plan-view scanning electron microscopy micrographs of annealed devices are shown in Figure 4.11. Large cracks are generated due to evaporation of the solvent used to deposit indium tin oxide deposited via electrochemical assistance and residual stress generated during annealing. The cracks act as charge barriers limiting or preventing charge collection across the top of the film. Another interesting aspect of the cracking is that the device containing quantum dots deposited using electrophoretic deposition and indium tin oxide deposited via electrochemical assistance (Figure 4.11B) does not show any correlation between the cracks in the nanotube array and the cracks in the indium tin oxide film; another indication that the indium tin oxide is not interfaced with the rest of the photovoltaic device.

46

4.2.5 Performance analysis of solar cells with electron beam evaporated indium tin oxide
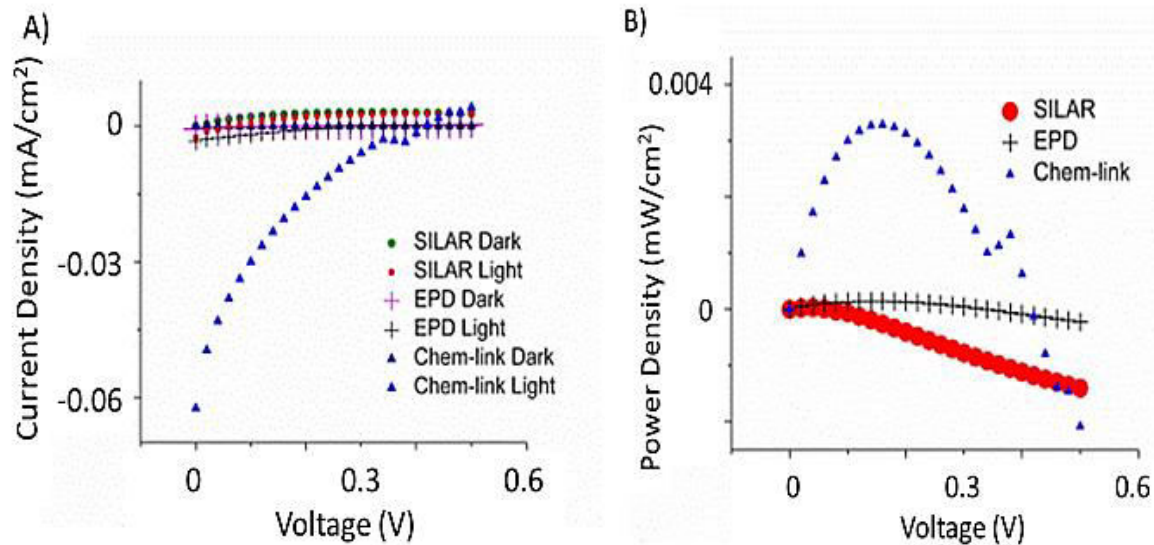
Figure 4.15 Typical current density (A) and power density (B) responses from nine replicates of photovoltaic devices containing TiO_2 nanotubes, indium tin oxide deposited via electron beam evaporation, and PbS quantum dots deposited using either successive ion layer adsorption and reaction, electrophoretic deposition, or chemical-linking

Electron beam evaporated indium tin oxide, which was deposited by thermal evaporation and subsequent condensation of an indium/tin target, does not involve the solution-based chemistry that led to the deleterious interactions with the quantum dots observed with indium tin oxide deposited via electrochemical assistance. Figure 4.15 displays the photovoltaic response of devices containing PbS quantum dots and indium tin oxide deposited via electron beam evaporation. Overall, the performance is greatly enhanced compared to that of devices containing indium tin oxide deposited via electrochemical assistance (Figure 4.12), but still below viable efficiency for use as commercial devices.

The observed enhancement could be attributed to a multitude of reasons. As seen in Figure 4.14, the concentration density of quantum dots remains unchanged after the deposition of

indium tin oxide deposited via electron beam evaporation for all devices, confirming that transitioning from the solution-based deposition of indium tin oxide deposited via electrochemical assistance to the vapor deposition of indium tin oxide deposited via electron beam evaporation prevented the detrimental dissolution of the PbS quantum dots. As the PbS quantum dots act as both the light harvester and as a physical barrier preventing charge-carrier recombination between the two-oxides, any technique that decreases damage to the quantum dots will enhance their ability to perform within the photovoltaic devices.

The topography of the indium tin oxide deposited via electron beam evaporation, displayed in the plan-view scanning electron microscopy images in Figure 4.11, is much more uniform than that observed with indium tin oxide deposited via electrochemical assistance, shown in Figure 4.10. Indium tin oxide deposited using electron beam evaporation shows only minimal cracking and no particulate-like formations. Since cracking and particle-to-particle percolation increase charge-trapping, the improved topography of the indium tin oxide deposited via electron beam evaporation also contributes to the enhancement of the photoresponse of these devices compared to those containing indium tin oxide deposited via electrochemical assistance. In addition to decreasing the number of potential charge-trapping sites, the reduction of cracking in the indium tin oxide deposited via electron beam evaporation device may also indicate a more complete indium tin oxide layer surrounding the quantum dots, which could limit air exposure of the quantum dots and increase the viable lifetime of the quantum dots as light-harvesters.
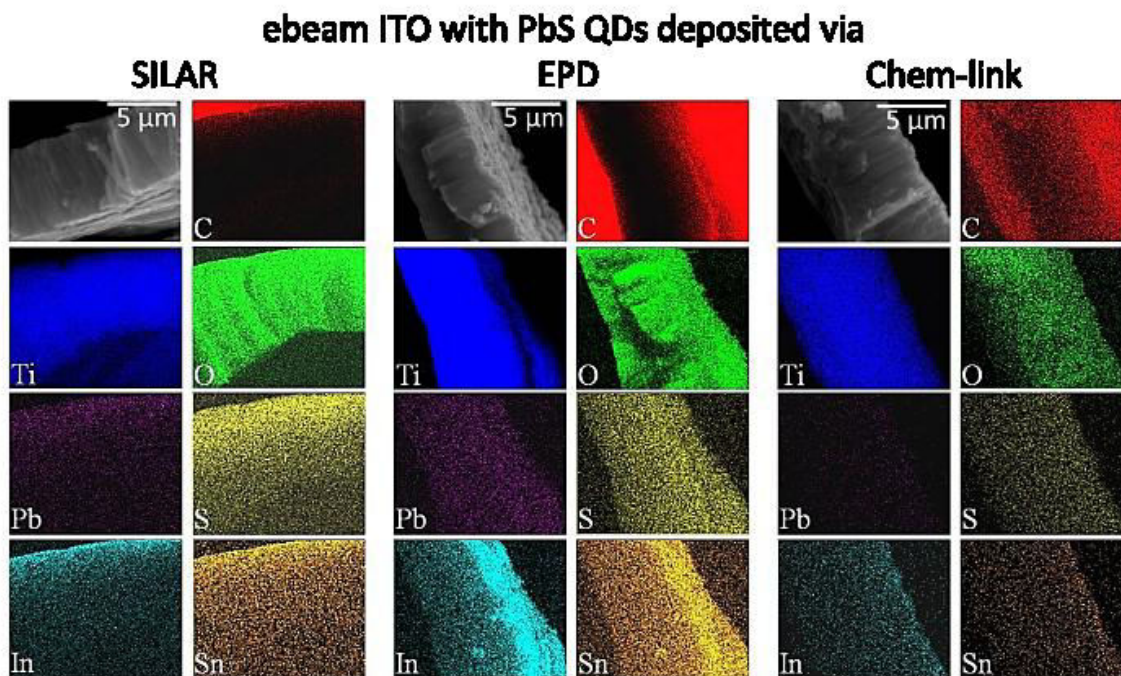
Figure 4.16 (Scale bar: 5 μm) Scanning electron microscopy-energy dispersive x-ray spectroscopy of photovoltaic side profiles with indium tin oxide deposited via electron beam evaporation and PbS quantum dots (QDs) deposited using successive ion layer adsorption and reaction (SILAR), electrophoretic deposition (EPD), or chemical-linking (chem-link)

Although evaporation of indium tin oxide reduces side-reactions associated with aqueous solution-based deposition and generates smoother films, evaporation from a point source can cause limited pore infiltration of materials into high-aspect-ratio structures. To evaluate the infiltration, scanning electron microscopy-energy dispersive x-ray spectroscopy maps of side profiles of indium tin oxide deposited via electron beam evaporation- containing devices (Figure 4.16) were analyzed. The low deposition rate of ~0.5 Å/s appears to allow infiltration of indium tin oxide into the pores in all of the devices. The device containing quantum dots deposited using electrophoretic deposition does still display some occlusion of the indium tin oxide, owing to the partial-sealing of the nanotubes by excess quantum dots. However, unlike indium tin oxide deposited via electrochemical assistance, indium tin oxide deposited via electron beam

49

evaporation does appear to infiltrate into the electrophoretic deposition quantum dot-functionalized nanotubes, likely due to the fact that hydrophobicity does not play a role during electron beam evaporation deposition.

4.3 Conclusion

The current work has shown that an all inorganic-solid state, quantum dot-sensitized photovoltaic can be fabricated and utilized to some efficiency with the highest efficiency devices being the ones containing quantum dots with uniform size and shape, ITO with ideal topography, and uniform infiltration of both the quantum dots and ITO, namely devices with chemically-linked quantum dots and electron beam evaporated ITO. The cells exhibit photo-generated power that varies depending upon the method used to deposit PbS quantum dots and ITO into the nanotube array. The various quantum dot deposition methods lead to differences in quantum dot morphology, nanotube occlusion, and quantum dot stability during ITO deposition. Optimization of these parameters is required to effectively harvest the maximum amount of sunlight.

Methods of depositing ITO included electrochemically-assisted deposition and electron-beam evaporation. Electron beam evaporation leads to higher efficiency devices for three prominent reasons: 1. Deposition conditions are less detrimental to the quantum dots; 2. The evaporated ITO infiltrates the nanotube array even if the nanotube array is partially sealed due to excess quantum dots at the surface; and 3. The topography of evaporated ITO is smooth and continuous with only minimal cracking.

While the difference between the quantum dot deposition techniques and the ITO deposition techniques generate substantial differences in the observed photovoltaic performance of the devices, the TEM images of quantum dots functionalizing nanotubes seen in Figure 4.3 pinpoint the root cause of the overall poor efficiencies and low fill factors of the devices—lack

of a continuous quantum dot layer. Quantum dots need to fully coat the nanotubes to provide optimal light absorption and to prevent recombination of charge carriers at oxide-oxide interfaces. However, generating a complete layer of quantum dots has proven difficult due to occlusion and agglomeration.

4.4 Future Work

Looking toward future optimal devices, combining the best device fabrication routes found here with recent advances in implementing quantum dots into solar-harvesting devices, which have come to rival the efficiencies of commercial Si and dye-sensitized solar cells, could be the archetype for future success. Bawendi constructed a PbS quantum dot thin film device with a certified efficiency of 8.55% [56]; it is not a typical quantum dot-sensitized solar cell, since charge generation and migration occur within the same material, but the meticulous bandgap engineering used to construct the device is similar to the energetic separation implemented in quantum dot-sensitized solar cell. It may just be possible that by employing the same bandgap engineering and equivalent materials into a quantum dot-sensitized solar cell that an even higher efficiency and better commercial-viability could be achieved, especially if self-assembly of ordered sizes of quantum dots are employed to make a rainbow, tandem cell configuration like that shown in the artistic rendition in Figure 4.17.
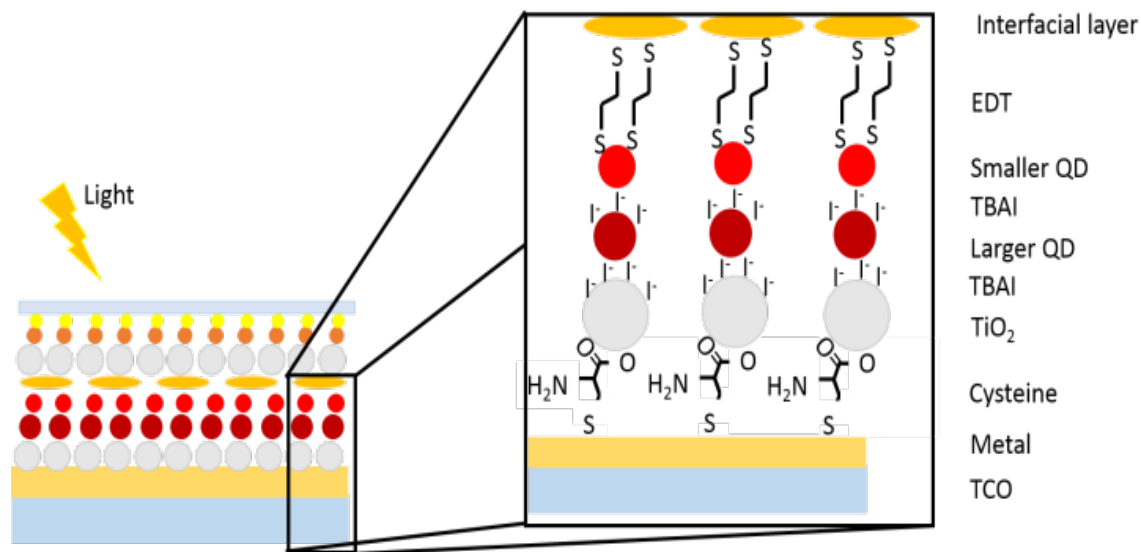
Figure 4.17 Artistic impression of quantum dot-sensitized solar cell utilizing ligand-modulated bandgap engineering, rainbow cell quantum dot size progression, and tandem cell design to maximize efficiency. From the bottom up the cell comprises a transparent conductive oxide substrate, coated with a metal contact, a self-assembled monolayer of cysteine, a single layer of TiO_2 particles functionalized with TBAI, a layer of TBAI-capped large size quantum dots, a layer of EDT-capped smaller size quantum dots, an interfacial layer, followed by the top cell which starting with the TiO_2 layer is identical the bottom cell with the exception that the quantum dots are smaller and the final structure is completed with indium tin oxide.

By utilizing a self-assembled monolayer of ligands on metal-substrates, for example cysteine which has been shown to facilitate charge migration in quantum dot-sensitized solar cell on Au[57], a single layer to a few layers of TiO_2 could be deposited through chemical-linking, limiting carrier recombination during percolation. The TiO_2 layer should be modified with an inorganic halide ligand, such as tertrabutylammonium iodide (TBAI), which Bawedi[56] utilized to create the bandgap offset ideal for charge separation, or one of the other commonly-utilized ligands to manipulate the quantum dot band structure[58,59] . The TiO_2 layer should then be decorated with a large-size quantum dot capped with the same inorganic halide and then with a

slightly-smaller quantum dot capped with a thiol, such as thioglycolic acid or 1,2-ethanedithiol (EDT), to further encourage charge separation through bandgap modulation, utilizing the well-known bandgap modulation through size adjustment[60,61] and the added benefit that larger size quantum dots have fewer accessible trap sites[62]. An interfacial layer, Au islands or conformal indium tin oxide film, separates the two cells. The entire cell should be completed with conformal film of indium tin oxide. Thus, the cell architecture facilitates charge-transfer similar to plants through physical and energetic separation of charge-carriers and takes advantage of enhanced solar collection through utilization of progressive sizes of quantum dots, like that of the Rainbow cell proposed by Kamat[63,64]. The other advantage of the prospective architecture is that it is a tandem cell, utilizing the power of multiple cells connected in series to improve the output efficiency[65]. The commercial-advantage of the prospective cell is that it is an easily-scalable, solution-based fabrication process that given the appropriate substrates could even be readily adapted to roll-to-roll processing [66] or cell printing[67]. The key to the efficiency demonstrated by photosystem I and potentially achievable with quantum dot-sensitized solar cell is the separation of carriers efficiently over macroscopic distances. The key for commercially-viable quantum dot-sensitized solar cell is the realization of this separation utilizing readily-abundant, cost-effective materials[68].

PART II: FERROELECTRIC PARTICLES FROM QUANTUM DOTS

CHAPTER V

FERROELECTRIC MATERIALS

5.1 Introduction

In 1920 Joseph Valasek presented his in-depth analysis of the unusual dielectric properties of Rochelle salt, which is deemed to be the first discovered ferroelectric material[69]. While scientifically intriguing, the fragile water-soluble salt did not lend itself to viable use in real-world applications. It would be twenty years before a viable ferroelectric material —barium titanate, which remains one of the most commonly study ferroelectric materials to this day— would generate mass interest in ferroelectricity[70]. Once ferroelectrics moved out of the realm of mere scientific curiosity, the depth of knowledge and number of known ferroelectric materials expanded rapidly. According to Varghese[69] the Landolt-Börnstein database lists 72 families of ferroelectric materials which are subdivided into three broad groups: 1) inorganic oxides, 2) inorganic non-oxides, and 3) organic crystals, liquid crystals, and polymers.

But what exactly is a ferroelectric material and why is it so intriguing? Ferroelectric materials possess a non-centrosymmetric, anisotropic unit cell. The asymmetric arrangement of the cations in respect to the anions within the crystal cell generates a dipole moment within that cell. Perturbation of these dipole moments by an external field leads to a poling of the material and an inversion of the atomic arrangement within the unit cell. Switchable polarization makes ferroelectric materials seemingly ideal candidates for use in non-volatile memory devices and other electronic applications[71, 72].

Just like research on many other materials used for electronic devices, ferroelectric material research has begun to investigate synthesis, characterization, and utilization of

nanoscale ferroelectric materials[71]. The synthetic procedures used to produce ferroelectric nanomaterials can be categorized into three broad groups: 1) chemical, 2) physical, 3) and biological[71]. Chemical techniques utilize chemical reactions to yield the desired product and are usually a solid-state, sol-gel, solvothermal, hydrothermal, or molten salt reaction[71]. Herein, we describe the utilization of a rarely, if ever, utilized chemical techniques-- cation exchange and doping-- to produce particles of a ferroelectric materials.

Efforts to improve the effectiveness of quantum dots for applications continue through the utilization of cation exchanges[73] and doping[74]. Building upon these efforts and following the literature precedent of Sb-doped CdSe thin films[75], this work presents the treatment of colloidal CdSe quantum dots with $SbCl_3$ as a synthetic strategy for producing Sb-doped CdSe quantum dots. Rather than self-limited exchange as predicted by the thin film work, a unique two-phase reaction is observed that yields highly-defective and thus highly-polarized CdSe, as well as Sb_xSe_y and $CdCl_2$. While $SbCl_3$ interactions with CdSe quantum dots as a fluorescence modifier[76] and ligand exchange molecule[77] have been reported, no previous literature describes the unorthodox exchange reaction and subsequent ferroelectric particles observed in the current work.[78]

Our straightforward synthesis of a ferroelectric has numerous possible applications in renewable energy[79], photodetection[80], and electrochemical cells[81] due to the unique physical and electrical attributes of the final product. Ferroelectrics belong to a subset of pyroelectrics, a division of piezoelectrics. Piezoelectrics possess a dynamic relationship between energy and crystal anisotropy that allows for their use in energy harvesting[82] and microelectromechanics[83]. Pyroelectrics, in addition to demonstrating piezoelectric properties, exhibit a non-zero net polarization that changes with temperature exploited in photodetection[84] and renewable energy[85]

technologies. Ferroelectrics possess all the mentioned properties for both piezoelectrics and

pyroelectrics, with the additional benefit of undergoing polarization reversal within an applied

field--making them ideal for use in memory and electrochemical devices[69] in addition to all the

applications as piezo- and pyroelectrics[71].

CHAPTER VI

EXPERIMENTAL METHODS

6.1 Preparation of Ferroelectric Precipitates

6.1.1 Synthesis of 4.3 nm oleic acid-capped CdSe quantum dots

Large (4.3 nm) oleic acid-capped quantum dots are synthesized by the techniques

discussed in Chapter 2 with the following adjustments. To limit concentration of the reactants

and the amount of TBP present in the reaction vessel, a 3 M Se:TBP solution (prepared by

combining 2.37 g Se in 10 ml TBP) was diluted with octadecene (ODE) to 0.2 M (66.7 µl of

stock solution diluted with 9.43 ml of ODE). Once the Cd-oleate reaction solution reached 290

°C, 10 ml of the 0.2 M Se:TBP:ODE was injected. The resulting quantum dots were allowed to

grow at 275 °C for 1 hour.

6.1.2 Synthesis of dodecylphosphonic acid-capped CdSe quantum dots

Dodecylphosphonic acid- capped CdSe quantum dots were synthesized as follows: 0.125

g CdO, 0.5 g dodecylphosphonic acid, 6 g hexadecylamine, 4 g of trioctylphosphine oxide were

stirred and heated to 320°C in a sealed 3-neck flask under argon flow. A temperature probe and

heating mantle were used to monitor and maintain appropriate heating conditions. To remove

excess water, the reaction vessel was purged using a 12-guage needle inserted into a rubber

septum until the reaction temperature reaches 150°C. Once the reaction reached 320°C, the

reaction solution was clear indicating the brown CdO has converted to colorless Cd-

phosphonate. At 320°C 3.5 ml of 0.2 M Se:TBP:ODE (preparation described in section 5.1.1)

was injected. The temperature was reduced to 275°C, and slowly the solution changed from clear

to yellow to red to brown. The reaction vessel was cooled using compressed air to below 90°C.

The resulting product was dispersed in toluene. To remove excess ligands and remaining

reactants, the product was washed using a series of precipitations and centrifugation. A small amount of the toluene-dispersed product was diluted with a large amount of methanol and spun at 6500 rpm for fifteen minutes. The resulting pellet contains the desired quantum dots and was retained; the supernatant contains excess ligands and unreacted starting materials and was decanted off the pellet and discarded. The pellet was dissolved in 3 ml of octanol and centrifuged at 6500 rpm for fifteen minutes. The supernatant contained the desired quantum dots and was retained. The pellet was discarded. The quantum dot solution was dispensed into clean centrifuge tubes and diluted with a large amount (25+ ml) of methanol. The solution was centrifuged at 6500 rpm for fifteen minutes. The clean pellet was diluted with hexanes.

6.1.3 Preparation of antimony trichloride solution

Antimony trichloride has a solubility of 62.8 g per 100 g of toluene[86], so the inorganic salt readily dissolved in toluene to prepare the reaction solutions. 2.5 mM solution of $SbCl_3$ was prepared by combining 60 mg $SbCl_3$ and 100 ml of toluene and shaking until all of the solid was dissolved.

6.1.4 Reaction of antimony trichloride and CdSe quantum dots

0.75 ml of 2.5 mM CdSe quantum dots in toluene was combined and shaken with 0.75ml of 2.5 mM $SbCl_3$ in toluene. Upon mixing, the suspended quantum dots fall out of solution. To investigate the reaction progress, samples of quantum dots were treated for one minute to investigate the start of the reaction and for twelve hours to investigate the completed reaction. The particles were purified to remove any excess unreacted materials by three cycles of centrifugation in toluene at 8 krpm for 1 minute followed by resuspension in toluene; cleanliness was monitored relative to the presence of Cl^- by reacting the supernatant after each cycle with $AgNO_3$ until a precipitate was no longer observed. The supernatant contains any unreacted

material, so it was discarded. The pellet was retained. For characterization, the clean pellet was separated into 0.01 g portions and dried under 30 mTorr vacuum for twelve hours. To observe translocation of the product in a non-polar solvent, the pellet was shaken with toluene until the particles were suspended; a gloved finger or hand-held Van de Graaff generator were brought into proximity of the particle container. The movement of the particles in response to the electric fields was photographed and filmed.

6.2 Characterization Techniques

6.2.1 Attenuated total reflectance- infrared spectroscopy

Attenuated total reflectance- infrared spectroscopy (ATR) is a modified infrared spectroscopy technique that reduces the difficulties associated with analyzing solid and liquid samples, namely sample preparation and spectral reproducibility. In ATR, an infrared beam is directed through a crystal with a high index of refraction at such an angle that the beam is completely reflected within the crstyal. As the beam is reflected within the crystal, an evanescent wave is generated and extends slightly (<5 μm) beyond the surface of the crystal. When the surface of the crystal is in intimate contact with a sample, the sample absorbs certain wavelengths of the infrared spectrum and in those regions the evanescent wave is attenuated. From these regions of attenuation, an infrared spectrum for the sample is created.

ATR was performed on a ThermoScientific Nicolet iS5 FT-IR spectrometer with iD5 diamond crystal ATR accessory on 0.01 g dried samples in range 600-4000 cm^{-1}. A background scan was taken between each sample. For controls, oleic acid and $CdCl_2$ were scanned. Cd-oleate was prepared following the synthetic procedure described in chapter 2 excluding the octadecene

and stopping before the addition of the secondary ligands. The as-synthesized Cd-oleate was cleaned and dried in the same fashion as the quantum dots prior to performing ATR.

6.2.2 Thermogravimetric analysis

Thermogravimetric analysis (TGA) is a technique used to monitor the decomposition or evaporation of materials. The mass of a sample as it is subjected to a heating program is carefully monitored. Temperature regions where the mass of the sample decreases indicate either evaporation or decomposition of a component within the sample. By comparing the temperatures at which mass loss is observed with the known boiling points and decomposition temperatures for likely substances contained within the sample, the composition of the sample can be determined.

TGA was performed on an Instrument Specialists' TGA-1000 with a platinum pan containing the dried sample and heated under a nitrogen flow of 90 sccm from 80-600°C with a heating rate of 20 °C/min and sampling rate of 1 Hz.

6.2.3 Scanning transmission electron microscopy and energy dispersive x-ray spectroscopy

As the name implies, scanning transmission electron microscopy (STEM) combines aspects of scanning electron microscopy and transmission electron microscopy. Like transmission electron microscopy, STEM correlates the intensity of electrons transmitted through an electron-transparent sample to create a grey-scale image of the sample. Like scanning electron microscopy, STEM rasters a focused electron beam across a sample, allowing spatial correlation of signals such as characteristic x-rays. Spatial correlation of characteristic x-rays is used to generate elemental maps of the sample. More information on energy dispersive x-ray spectroscopy can be found in chapter 2.

Cleaned samples in toluene were shaken to suspend the particles and a drop of the solution was place on an ultrathin carbon TEM support film (Ted Pella 1822-F) held by anticapillary tweezers. Excess solvent was wicked away using a Kimwipe®. The as-prepared samples were imaged and analyzed on a FEI Tecani Osiris STEM with approximately 1 nA of beam current. Elemental maps were prepared using signals from scanning points that register within the narrow (55%) peak area of Sb-Lα (3.603 eV), Cd-Lα (3.132 eV), Se-Kα (11.210 eV), and Cl-Kα (2.621 eV). Atomic weight percent of each element was calculated in Bruker Esprit 1.9 from the integrated spectra using the Cliff-Lorimer ratio method.

6.2.4 Sawyer-Tower hysteresis loops

Polarization response was measured utilizing a sandwich cell consisting of two indium tin oxide-coated glass slides separated by a 20 µm spacer with an active area of 0.19 cm^2, compressed around a concentrated paste of the particles in n-heptane[87]. The sandwich cells were connected into the traditional Sawyer-Tower circuit with a triangular waveform of ±10 V applied to the circuit. The voltage input and the voltage drop across a 4.7 µF reference capacitor in series with the cell were used to determine the polarization and electric field across the samples.

To prepare the sandwich cell, two ITO glass slides were cleaned by sonication in 0.3% soap solution, then acetone, then isopropanol followed by drying with nitrogen. A 20 µm spacer with 0.19 cm^2 active area was prepared by using a hole punch to remove a circle from a 2 inch square of Vibac™ Sealast tape. To remove the adhesive, the tape was soaked for fifteen minutes in hexanes, leaving only a 20 µm thick sheath. The sheath was wrapped around an ITO slide and held taut as the 0.01 g portion of dried sample is placed in the active area. The sample was compressed and spread over the active region by placing the second ITO slide over the area and

compressing. To ensure connectivity a drop of isotropic n-heptane was added to the sample and the cell was secured with binder clips.

The cell was connected in series with a 4.7 µF reference in the traditional Sawyer-Tower circuit. A ±10V triangular waveform is applied to the circuit at a frequency of 0.5 V/s using a Keithley power source. Channel 1 on an oscilloscope monitored the voltage input by connecting across the electrodes of the Keithley; the electric field across the sample was taken as the quotient of the voltage input and the thickness of the sample. Channel 2 of the oscilloscope measured the voltage across the reference capacitor by connecting across the terminals of the capacitor. The charge across the reference capacitor was calculated as the product of the reference capacitance and the voltage across the reference capacitor. Since the reference capacitor was in series with the sample, this charge was equivalent to the charge across the sample. The polarization of the sample was calculated as the quotient of the charge and the active area of the electrodes.

FERROELECTRIC PARTICLES

7.1 Reaction Dynamics

Upon combining the quantum dots and the $SbCl_3$, the particles flocculated together but remained suspended in the non-polar solvent. As time progressed, the flocculates became much larger (up to 100+ μm) and precipitated out of solution, as shown in Figure 7.1.
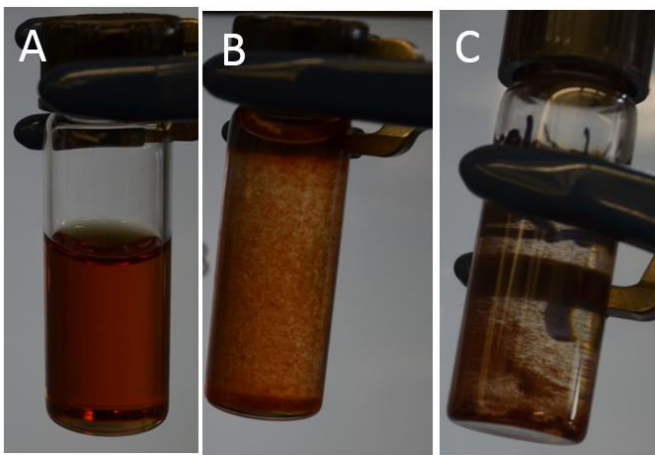
Figure 7.1 Photos of CdSe quantum dots (A) treated with $SbCl_3$ for 1 min (B) and for 12 hrs (C).

CdSe treated for 1 min shows small agglomerates flocculating together suspended in toluene; whereas, the CdSe treated for 12 hrs displays large agglomerates precipitated out of toluene.

To find the source of the two observed phases of flocculation, scanning transmission electron micrographs with energy dispersive x-ray spectroscopy elemental maps (STEM-EDS), ATR-IR, TGA, XRD, SEM-EDS, and ICP-OES are performed on untreated CdSe quantum dots and CdSe quantum dots treated with $SbCl_3$ for one minute and for 12 hours.
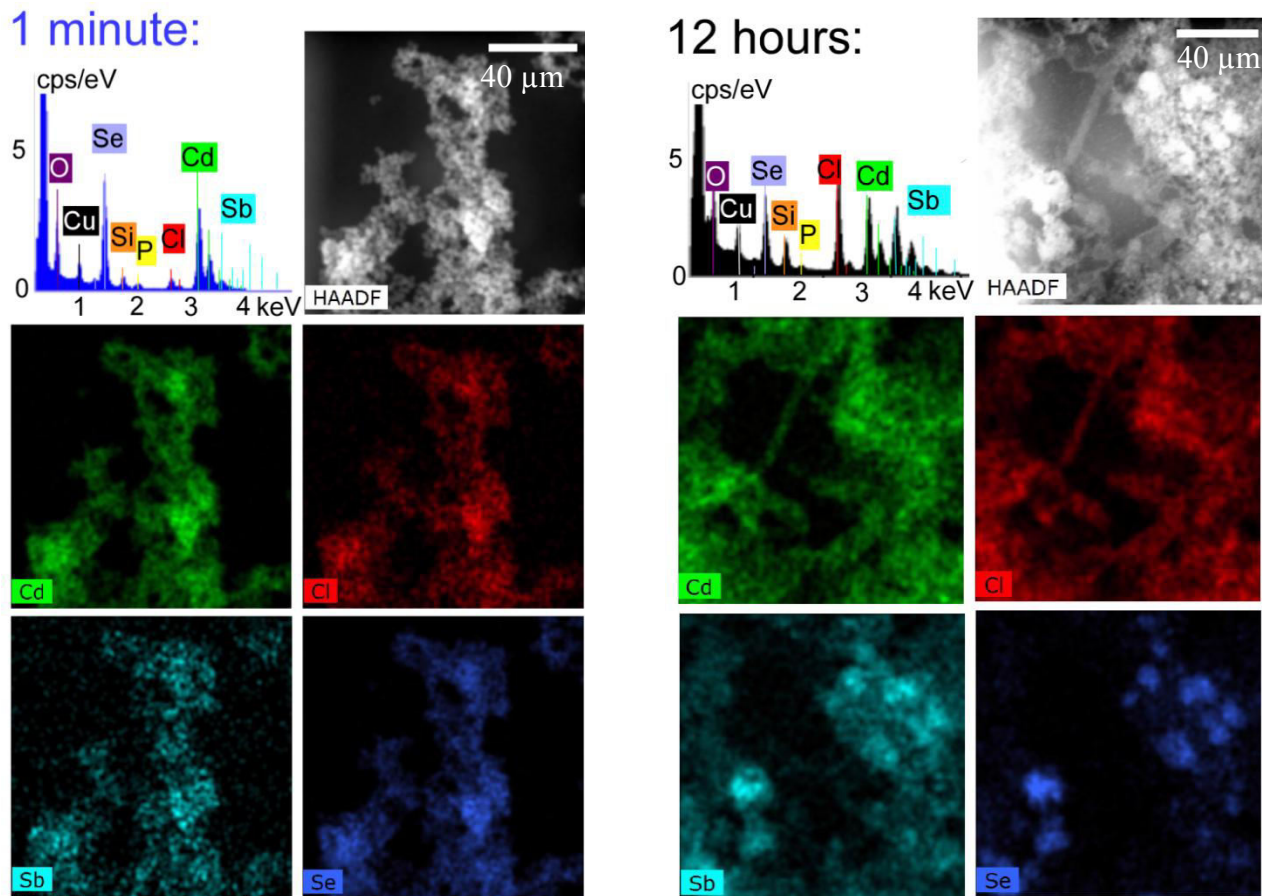
Figure 7.2 STEM HAADF image, EDS spectra, and elemental maps of CdSe quantum dots treated with SbCl$_3$ for 1 min and for 12 hrs. 1 minute sample shows Cl around CdSe quantum dot agglomerates. 12 hour sample shows Cd and Cl surrounding particles containing Sb and Se. Scale bars: 40 μm

STEM-EDS maps and spectra of CdSe quantum dots treated with SbCl$_3$ for one minute and for twelve hours, shown in Figure 7.2, elucidate the two phases of the reaction that produced the ferroelectric particles. An initial ligand disruption and replacement by Cl$^-$ was readily observed in the sample treated for one minute. Cl is co-localized with the agglomerates of CdSe; however, individual quantum dots were still distinguishable, and a very low Sb signal barely above noise level was detected in the spectrum. The second phase is an unbalanced cation-exchange observable in the sample treated for twelve hours as an overlap of the x-ray signals for

Cd and Cl within a matrix surrounding overlapping signals from Sb and Se. The maps indicated the probable formation of $CdCl_2$ and Sb_2Se_3 as predicted by the reaction shown in Rxn 7.1.
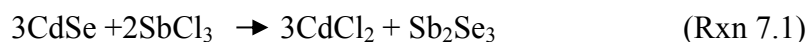
$$3CdSe + 2SbCl_3 \rightarrow 3CdCl_2 + Sb_2Se_3 \qquad \text{(Rxn 7.1)}$$

However, energy dispersive x-ray spectroscopy and inductively-coupled plasma optical emission spectroscopy indicate the ratio of Sb:Se is close to 0.4, well below the 0.67 needed for a charge-balanced compound. Also, the x-ray diffraction pattern (Figure 7.3) of treated quantum dots displayed sharp peaks that with an 80% confidence level to $CdCl_2$ in the peak matching program DMSNT ICDD (1997). In conjunction with the elemental information, the final products appear to be residual CdSe quantum dots, amorphous Sb_xSe_y, and $CdCl_2$.

The two-phase reaction mechanism was further supported by ATR-IR analysis shown in Figure 7.4. ATR-IR absorption spectrum of CdSe quantum dots showed the expected peaks for CdSe capped with oleic acid as reported previously[88] with the extended scan showing the C-H stretches of oleic acid just below 3000 cm^{-1}. The spectra of CdSe quantum dots treated for one minute with $SbCl_3$ displayed a material in transition with a pronounced decrease in the peak height and sharpness due to disruption and removal of some of the surface- capping oleic acid groups. The emergence of a small peak at 1588 cm^{-1} foreshadowed the secondary reaction that produced $CdCl_2$, which was clearly seen in the sample treated for 12 hours by the sharp peak at 1588 cm^{-1} and the doublet centered at 3500 cm^{-1}.

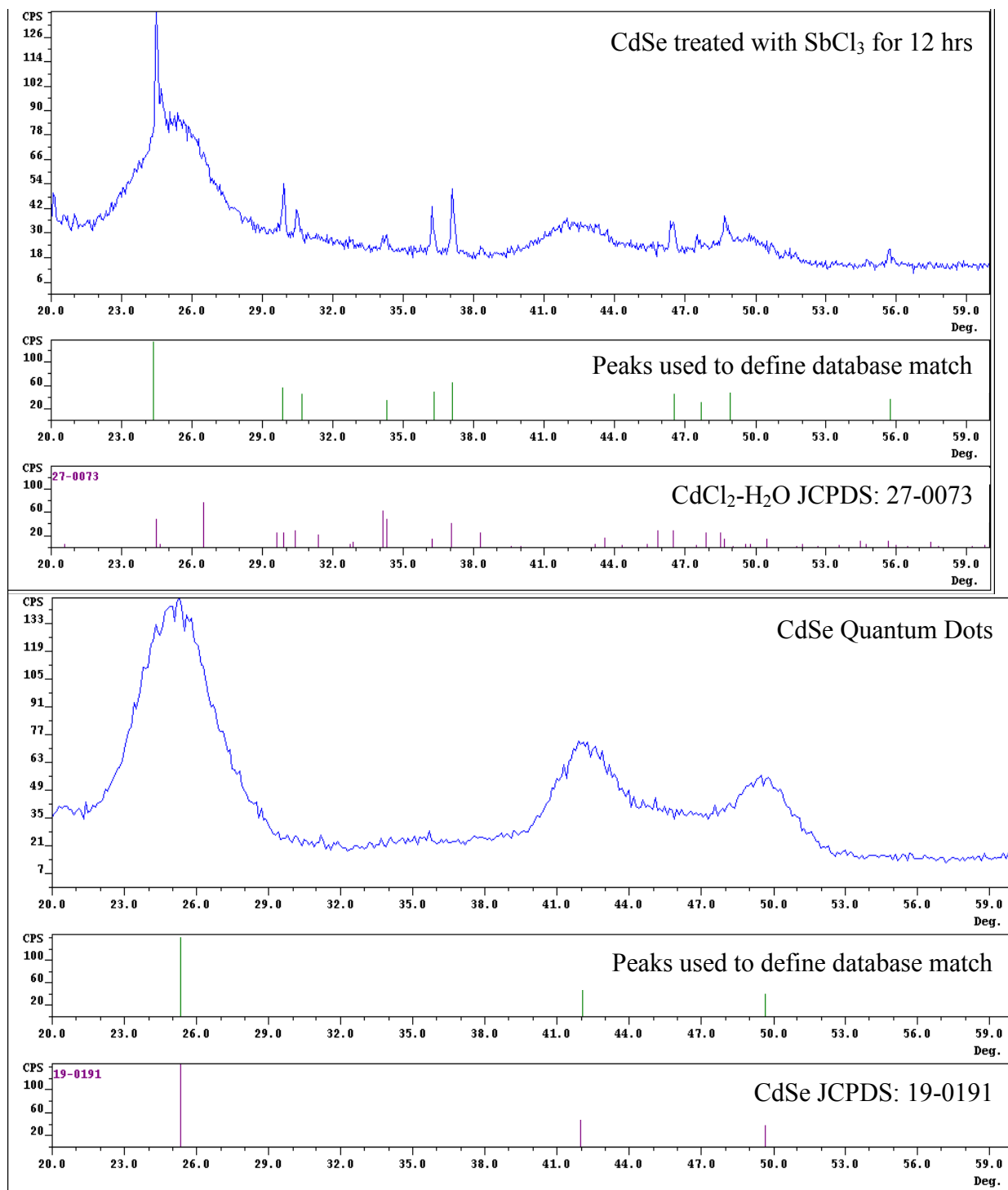Figure 7.3 XRD with DMSNT ICDD (1997) compound matches of CdSe SbCl$_3$-treated for 12 hrs (top) and CdSe quantum dots (bottom) on (500) Si; CdSe quantum dots display the typical broad peaks associated with wurtzite CdSe quantum dots (JCPS 19-0191). SbCl$_3$-treated CdSe reveals crystalline structure of CdCl$_2$-H$_2$O (JCPDS 27-0073) and but no discernable features of crystalline Sb$_2$Se$_3$ (JCPDS 15-0861).
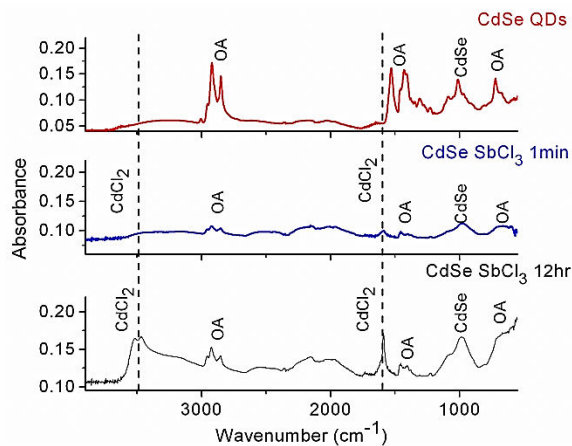
Figure 7.4 ATR-IR of CdSe quantum dots and CdSe quantum dots treated with $SbCl_3$ for 1 minute and for 12 hours, showing the disruption and partial loss of oleic acid followed by the production of $CdCl_2$ (dotted lines indicate $CdCl_2$ peak locations).

TGA curves, displayed in Figure 7.5, indicated mass loss for the untreated CdSe quantum dots began slowly at 220 °C, peaked at 477 °C, and plateaued at 530 °C. Previous TGA studies[89] of CdSe quantum dots capped with organic ligands indicate a range comparable to the one observed here for the loss of surface ligands. Quantum dots treated with $SbCl_3$ for 1 min and for 12 hrs displayed much lower mass-loss within this initial temperature range due to the disruption and removal of the capping-oleic acid ligands by Cl^-. A second interval of mass-loss starting at 490 °C was observed for the treated samples and was attributable to the sublimation of $CdCl_2$[90].
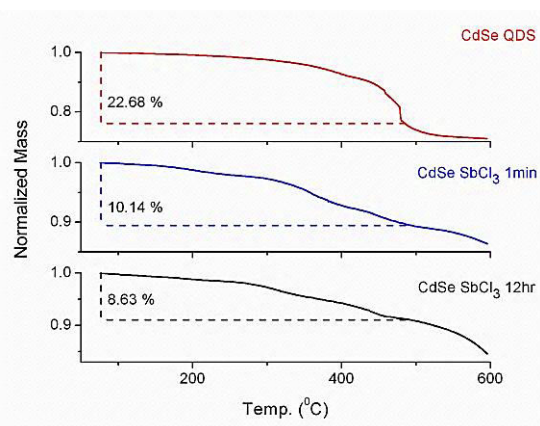
Figure 7.5 TGA comparing untreated CdSe quantum dots to CdSe treated with $SbCl_3$ for 1 minute or 12 hours, revealing fewer ligands on the treated samples and production of $CdCl_2$

7.2 Ferroelectric Properties

7.2.1 Particle translocation within an electric field

The treated particles demonstrated extremely large net polarizations, sensitive enough to migrate in response to the electric field generated by a gloved finger as seen in Figure 7.6.
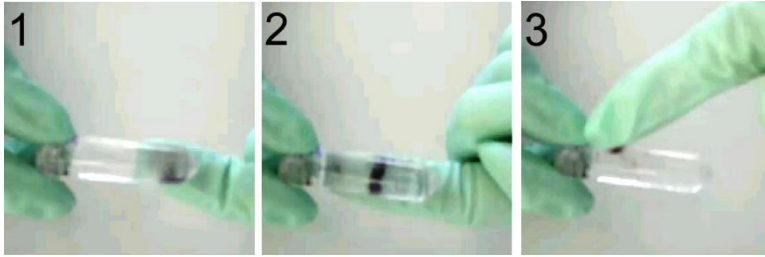
Figure 7.6 Photo series of SbCl$_3$-treated CdSe particles translocating in the electric field generated by a gloved finger

7.2.2 Polarization response
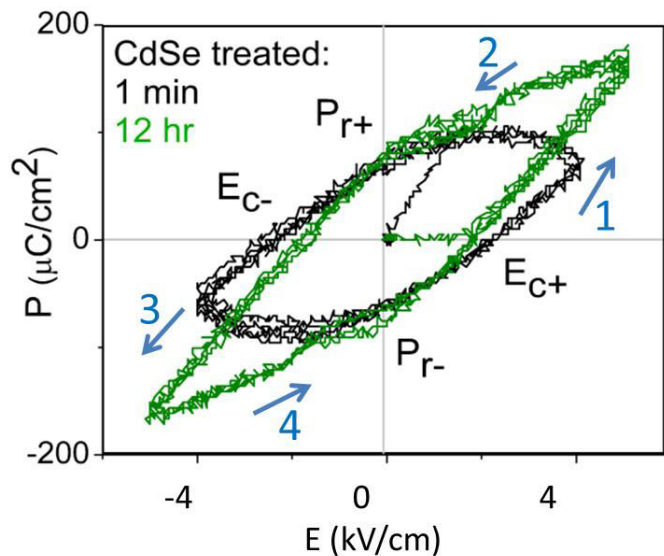
Figure 7.7 Polarization response within an applied electric field for CdSe quantum dots treated with SbCl$_3$ for 1 minute and for 12 hours; remnant polarization (Pr) and coercive electric field (Ec) shown

Within a sweeping electronic field, SbCl$_3$-treated CdSe displayed an obvious hysteretic behavior, a signature of ferroelectrics; results shown in Figure 7.7. The maximum remnant

polarization (P_r) of 80 µC/cm^2 and a coercive electric field (E_c) of 2 kV/cm obtained with the sample treated for 12 hours are comparable to other known ferroelectrics, notably BiFeO$_3$[91], BaTiO$_3$[92], and PbTiO$_3$[93].

The dramatic decrease in the initial susceptibility (the linear portion starting at 0V during the first sweep of the field response curves shown in Figure 7.7) from the sample treated for 1 minute to that of the sample treated for 12 hours can be attributed to a disruption and slowing of ferroelectric domain nucleation and switching in the sample treated for 12 hours due to the presence of Sb$_x$Se$_y$ and CdCl$_2$. The added materials act as electronic defects preventing an even field distribution throughout the device and as physical barriers preventing tangential ferroelectric grains from coalescing or facilitating in turnover with one another. Thus, a larger coercive field is necessary to generate the initial polarization alignment. While the initial susceptibility is negatively impacted, the saturation polarization (maximum level of polarization achieved) increases from 96 to 120 µC/cm^2. The observed increase in polarization is unsurprising given the two new materials within the active region possess electronically-active structures. Luby *et al.* discuss the electronic switching phenomena observed for amorphous samples of Sb$_x$Se$_y$; the analysis of current-voltage responses display a characteristic switch from high-resistivity to low-resistivity states from Sb$_x$Se$_y$ films[94]. The switching is attributed to the generation of a conduction channel through the sample due to electrothermal processes. Anisotropic anomalies arising within layer structures is also a well-known phenomenon discussed extensively for Cd-containing layer-structures by Van der Valk *et al*[95]. Asymmetric coordination of anions with a highly-charged cation produces polarization of the anions, which in an ideal octahedral complex of a metal ion surrounded by anions, the overlap repulsion and covalent bonding yield isotropic fields. However, introducing defects to the ideal octahedral,

which given the random-nature of our reaction is likely, yields an increased anisotropy that could contribute to the observed polarization effects in our samples.
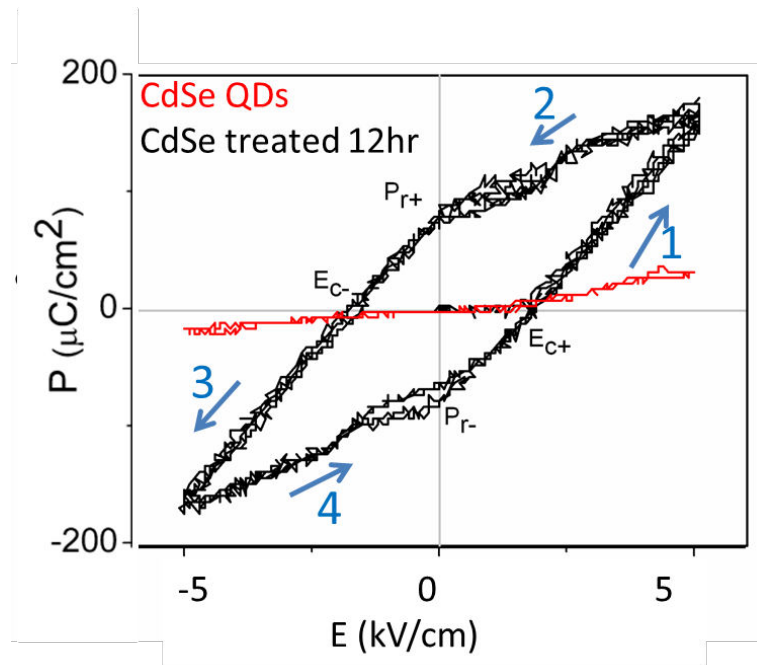
Figure 7.8 Polarization response in an applied electric field for CdSe Quantum dots and CdSe Quantum dots treated with $SbCl_3$ for 12 hrs; remnant polarization ($P_{r+,-}$) and coercive electric field ($E_{c+,-}$) shown

Untreated CdSe quantum dots responses are shown in Figure 7.8 and display a closed loop with no remnant polarization (the polarization of the cell is always zero when the applied field is zero). CdSe is a thermoelectric with a spontaneous polarization reported[96] to range from 0.2-0.6 $\mu C/cm^2$, which is too small to be observed in the unamplified signals collected in this study.

7.3 Conclusion

In absence of a detailed structural arrangement, we can offer a hypothesis on the origin of the ferroelectric properties based on the experimental results and literature resources about polarization in CdSe. From the indicated two-phase reaction and formation of mesoscale superstructures, the observed non-zero net polarization response is attributed to the exodus of Cd^{2+} from CdSe quantum dots during treatment with SbCl3 resulting in anisotropic, charge-imbalanced species. The assembly of nanoscale objects into large superstructures is key in mesoscale science; a branch of science wherein the broken symmetry of heirarchial structures is attributed to the generation of novel properties not observed in the nano- or bulk- phases of the material[97].

Cation exchange is a versatile technique that has allowed the formation of a variety of nanostructures[73, 98-100]. Postsynthetic modification of nanostructures by tuning the ratio and nature of the cations has allowed manipulation of many of the properties of the nanostructures from photoluminescence[100, 101] to geometry[98,102]. The current work utilizes a cation exchange to produce ferroelectric particles. The ferroelectric response is observable within 1 minute of treatment and arises from the deviation of pyroelectric CdSe from its ideal near-stoichiometric ratio. As observed in the STEM-EDS maps, an exodus of Cd ions out of the quantum dots occurs.

Overtime, Sb^{3+} integrates within the resultant charge-imbalanced Se-structures while the Cd^{2+} reacts with Cl^-. However, energy dispersive x-ray spectroscopy and inductively-coupled plasma optical emission spectroscopy shown in supplementary information indicate the ratio of Sb:Se is close to 0.4, well below the 0.67 needed for a charge-balanced compound. The unrequited charge imbalance and distortion of CdSe structure results in a highly anisotropic

structure that demonstrates a non-zero net polarization. As discussed by Shaldin *et al.* when the composition of CdSe deviates from the ideal, defect centers form leading to local asymmetry[103]. From an atomistic point-of-view, Shaldin *et al.* discusses the introduction of local anisotropy within the crystal structure of CdSe. The basic structure is described as two deformed tetrahedral systems of $CdSe_4$ and Cd_4Se. If the central atom is changed, local symmetry remains unchanged and the inherent polarity of the two subsystems is retained. However, if the bases of the tetrahedra possess a vacancy or if an interstitial atom is introduced into the structure, the symmetry of the subsystem is lowered and 3 new vectors of polarization are introduced. The atomic defects within $SbCl_3$-treated CdSe quantum dots arise from the introduction of Cd-vacancies and Sb^{3+} interstitials which results in the highly-polarized, anisotropic structures.

7.4 Future Directions

Preliminary studies shown in Figure 7.9 have indicated a distinct difference in the exodus of Cd out of the quantum dots depending on the surface ligand and/or crystal structure. With oleic acid-capped, zinc blende CdSe quantum dots the direction of Cd expulsion appears random. However, with dodecylphosphonic acid- capped, wurtzite, Cd appears to preferentially exit from the cation-rich facets. Studies into the reaction dynamics and theoretical modeling will shed light on the observed difference and impact that surface ligands and crystal structure have on quantum dot reactivity and doping. If particle doping can be tuned using surface ligands or crystal structure, scientist may have a unique tool to develop a variety doped quantum dots, such as Janus-like anisoptropic or radially-doped particles.
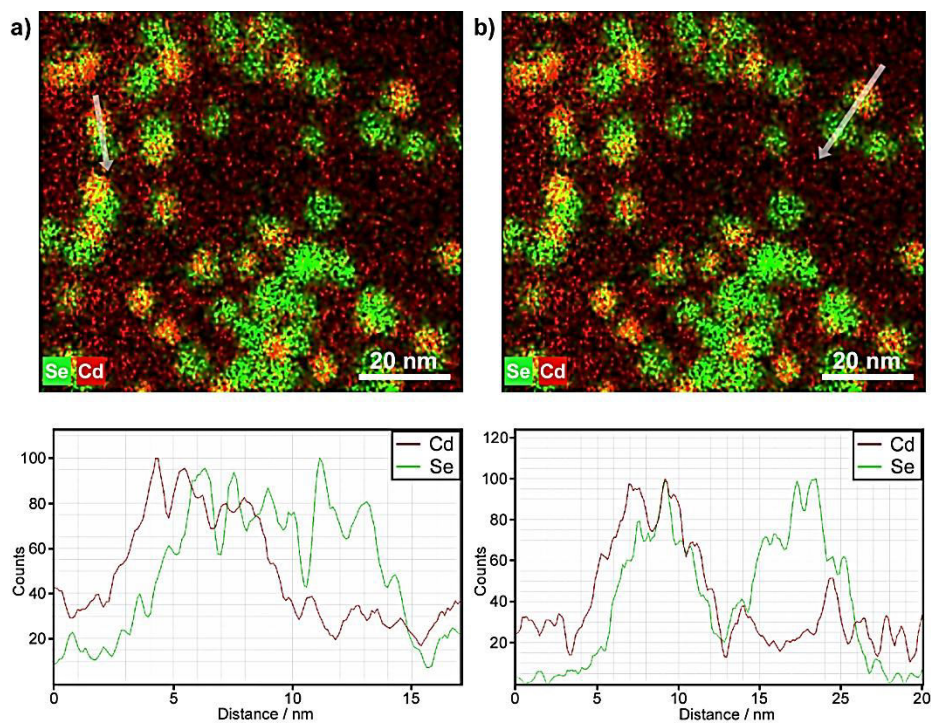
Figure 7.9: Scanning Transmission Electron Microscope Energy Dispersive X-ray Spectroscopy Elemental Maps of dodecylphosphonic acid-capped CdSe treated with antimony trichloride (a) depicts an aggregate and (b) solo quantum dots each displaying similar compositional heterogeneity

APPENDIX A

FRONTSIDE ILLUMINATED PHOTOVOLTAICS

A.1 Characterization and Performance

To fabricate a front side illuminated device, the nanotubes are anodized with same

parameters as described in Chapter 3, but at the conclusion the nanotubes are lifted either using

high voltage pulses[104] or water[105]. Due to issues with breaking when high voltage pulse is used,

all the devices tested thus far have been water lifted. After lifting, the nanotubes are transferred

onto an FTO glass slide that has a thin layer of TiO2 particle paste spun-cast onto it. While the

particle paste has been used successfully in literature[106], it may be one of the factors limiting the

efficiency of the devices. The particle layer is a network of TiO2 particles, which means that

electrons may become trapped in localized percolation in this region. An alternative method that

will be used on future devices is using a Ti-isopropoxide solution to form linkages directly

between the nanotubes and the FTO[106]. After the nanotubes are placed onto the FTO slide,

everything is annealed in a tube furnace using the same parameters as back-side illuminated

device. After the nanotubes are annealed, they are sensitized with quantum dots and covered with

hole conductor in same fashion as the backside illuminated devices. The back contact for the

tested devices has thus far been thermally evaporated aluminum.

The finished devices are tested under simulated solar emission. Most of the devices tested

were tested in Dr. Nathaneal Smith's laboratory at Middle Tennessee State University. Dr.

Smith's testing set-up uses a continuous emission, UV-filtered xenon-arc lamp to simulate the

solar spectrum. The set-up is calibrated using an Oriel Reference Solar Cell and Meter so that at

the desired testing distance the tested device receives power input of 1000W/m^2, the equivalent

power of one sun striking the earth's surface. The device is wired to a Keithley Power Supply

that is controlled by a voltage sweep MatLab program.
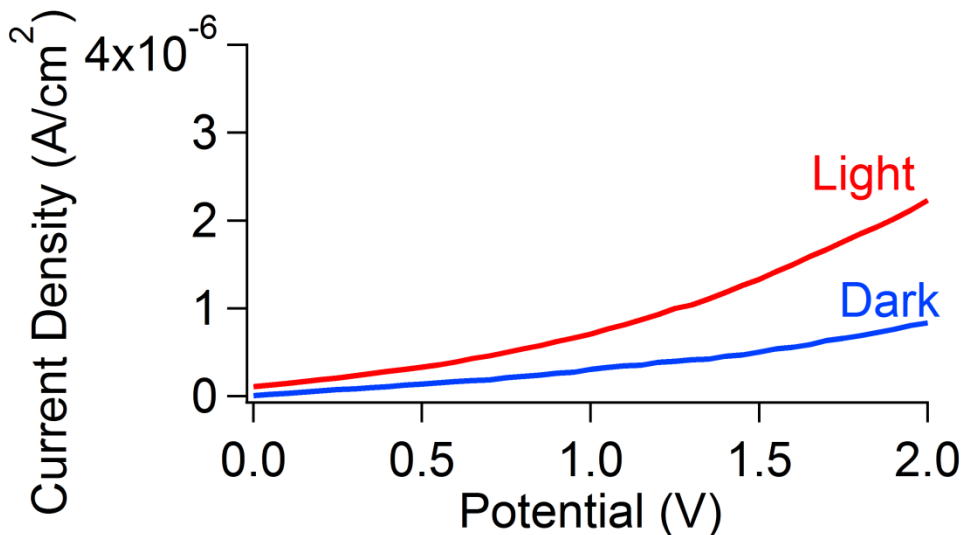
Figure A1. Photovoltaic response of frontside illuminated device

Typical photovoltaic response for frontside illuminated devices are shown in Figure A1.

The results show the usual p-n junction response curve; however, no power is generated by the

device. It is possible that not enough quantum dots are available or able to generate a photo

response. Optical transmittance measurements obtained at various points during device

fabrication are shown in Figure A2. The extinction curve of P3HT overwhelms that of the CdSe

quantum dots; this is an indication that perhaps the P3HT is absorbing a majority of the light.

The increase in transmission of light around 650 nm through the nanotubes after

application of quantum dots is attributed to a decrease in Rayleigh scattering from the nanotube

surface. Scattering of light prior to reaching the quantum dots is another possible reason for low

efficiency observed in the devices. However, the reflectance off the device shown as purple line

in Figure A2 indicates that minimal scattering is occurring in the UV and visible regions.
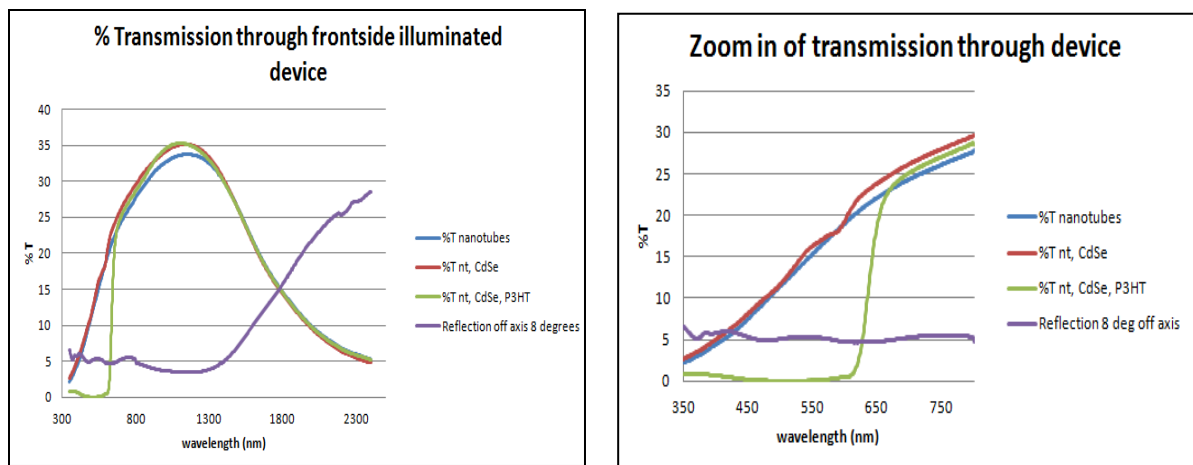
Figure A2. Optical transmission through and reflection (purple line) from a frontside illuminated device

APPENDIX B

OPTMIZATION OF ELECTRON BEAM EVAPORATED INDIUM TIN OXIDE

B.1 Characterization and Performance

To determine the optimal post-synthetic treatment for electron beam evaporated indium tin oxide (ITO), ITO thin films (40 nm) were deposited on glass slides. Subsequently the films were annealed in ambient air at various temperatures. The resistivity and transmittance of films annealed at 180, 250, 375, and 450 °C for 3 hours are shown in Figure B1. As the light passes through the ITO prior to interacting with the quantum dots in the photovoltaics, the ITO must demonstrate a high transmission with a low resistivity. The highest transmissions were obtained with 375 and 450 °C; however, those temperatures also reflect the highest resistivities. Since the TiO_2 nanotubes need to be annealed at 450 °C to crystallize the nanotubes into anatase and the properties of ITO are not extremely improved by lower temperatures, 450 °C was selected to be the anneal temperature for photovoltaic devices.
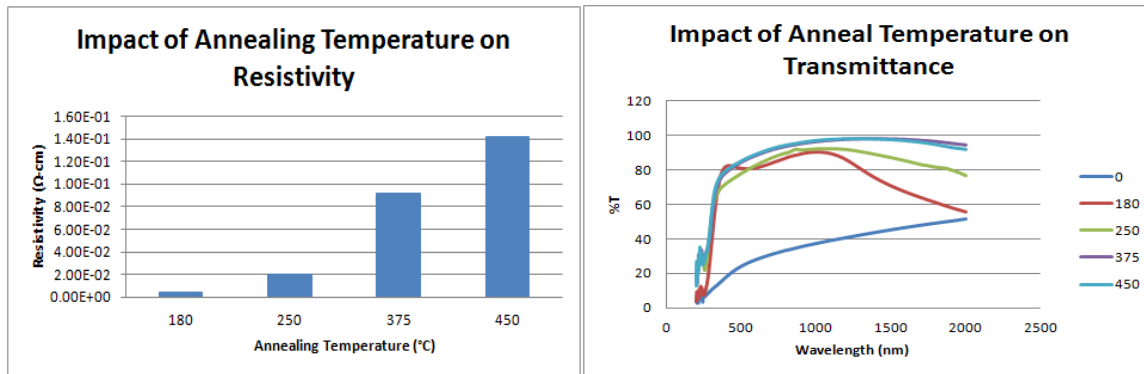
Figure B1. Resistivity (left) and transmittance (right) dependence on annealing temperature of electron beam evaporated indium tin oxide

To determine the duration of time needed to anneal electron beam evaporated ITO, 40 nm thin films deposited on glass were annealed at 450 °C for 0 hours (not annealed), 1 hour, and 3 hours. The resistivity and transmittance shown in Figure 4B indicate that 3 hours of annealing creates the low resistivity and high transmittance desired for the photovoltaic devices.
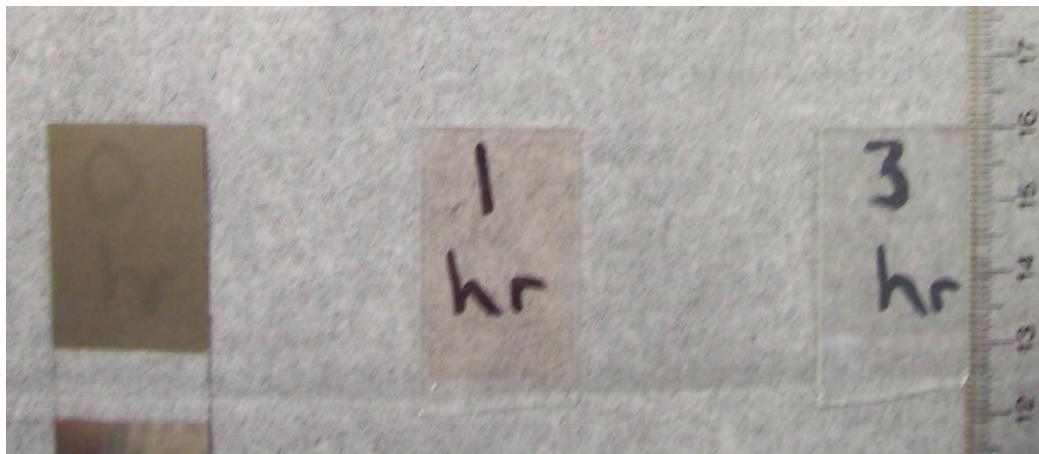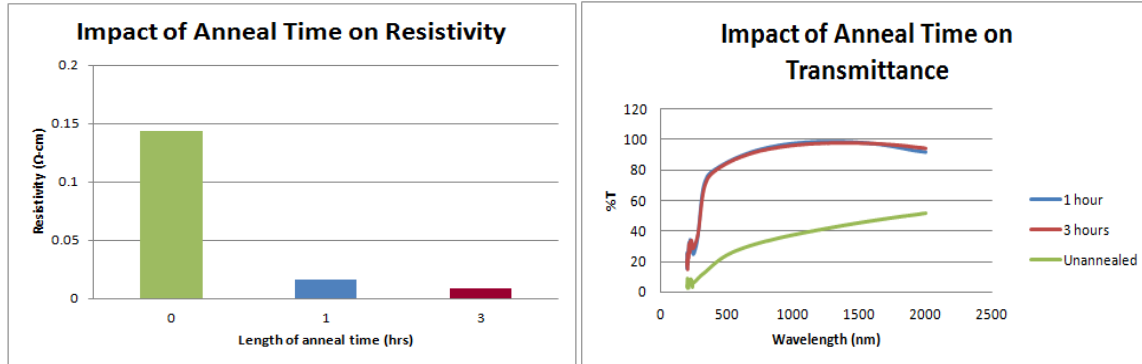
Figure B2. Resistivity (top left) and transmittance (top right graph and bottom photo) dependence on anneal time

ZnS BARRIER LAYER

C.1 Characterization and Performance

Previous photovoltaics with the architecture displayed in Figure C1 appeared to suffer efficiency losses from charge recombination due to contact between the ITO hole-conducting material and the TiO_2 electron transport material.
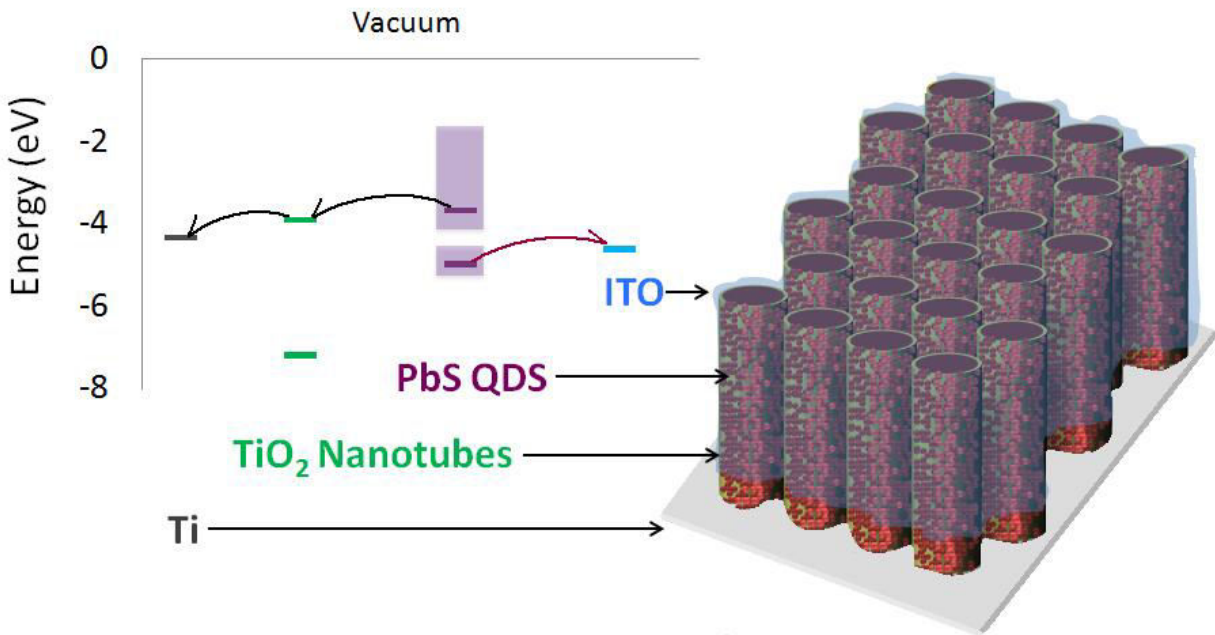
Figure C1. Photovoltaic architecture and energy diagram

A ZnS barrier layer has been successfully utilized to reduce interfacial charge recombination in previous photovoltaic research[107, 108]. A ZnS barrier layer was incorporated between the quantum dot layer and the ITO to prevent electron transport from the PbS or the TiO_2 to the ITO as shown in Figure C2.
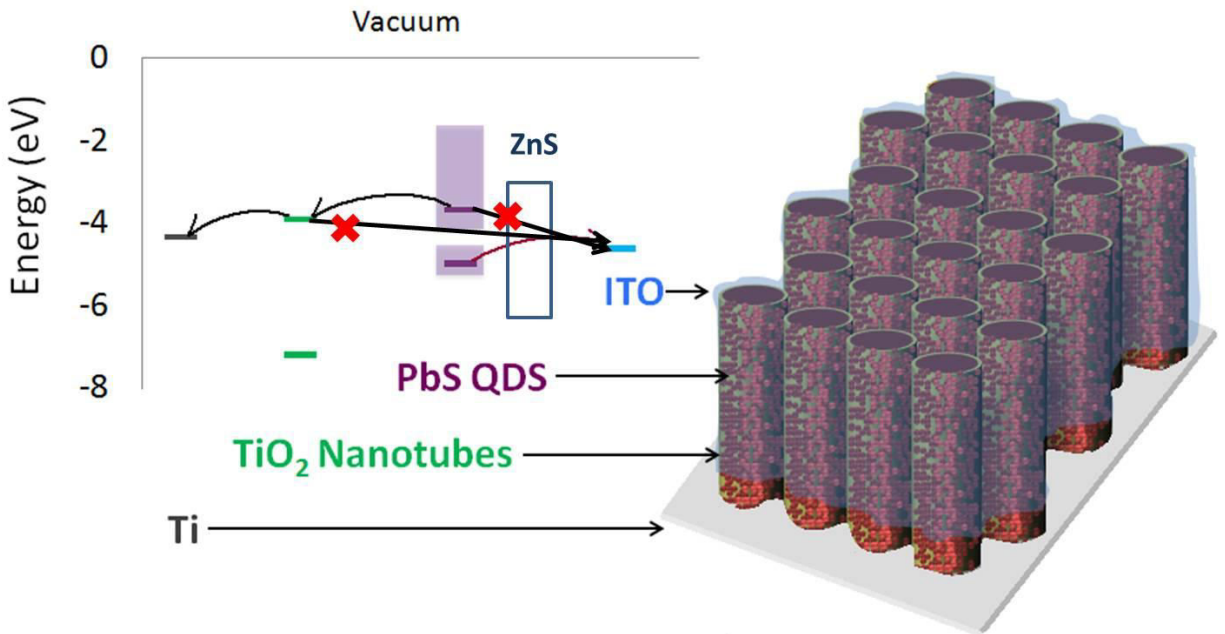
Figure C2. Photovoltaic architecture and energy diagram showing the impact of ZnS barrier layer

To deposit the ZnS layer the well-established successive ion layer adsorption and reaction technique was employed[108]. In short, the quantum dot-functionalized nanotube array was dipped into a 0.1 M solution of Zn-acetate in methanol for 1 min, rinsed with methanol for 1 min, dipped into a 0.1 M solution of NaS_2 in methanol for 1 min, and rinsed with methanol for 1 min. Unfortunately, the efficiency and figures of merit (Figure C3) of photovoltaics containing ZnS were lower than those previously observed.
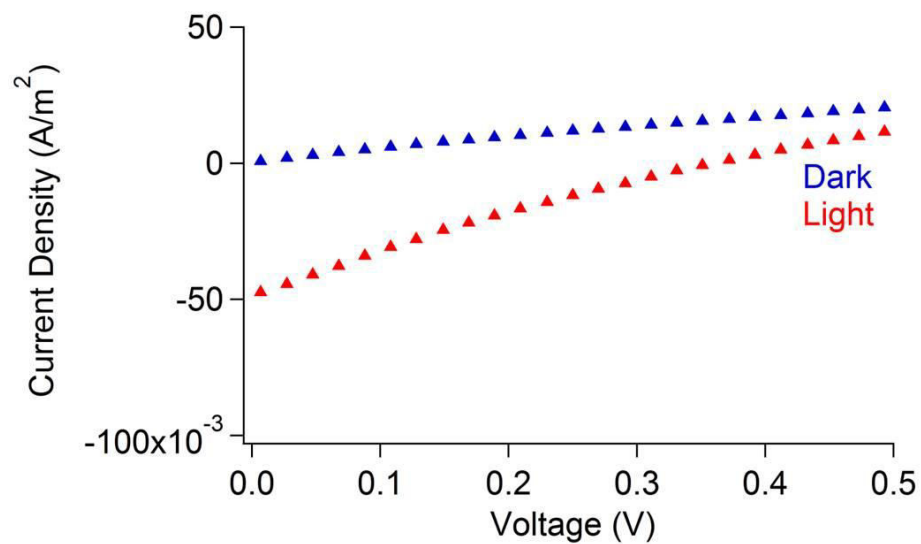
ZnS barrier layer	n	J_{sc} (A/m²)	V_{oc} (V)	FF	Eff (%)
Not present	9	-0.5 ±0.3	0.40 ±0.01	0.16 ±0.06	(3.3 ±0.5) x10⁻³
Present	9	-0.05 ±0.02	0.35 ±0.02	0.22 ±0.07	(3.7 ±0.3) x10⁻⁴

Figure C3. Photovoltaic performance and figures of merit (Jsc- short-circuit density, Voc- open circuit voltage, FF-fill factor, and eff- efficiency) of devices containing ZnS barrier layer

Scanning electron microscope images (Figure C4) of devices indicated occlusion of the

ZnS and ITO to the tops of the nanotubes is the cause for the decrease in efficiency.
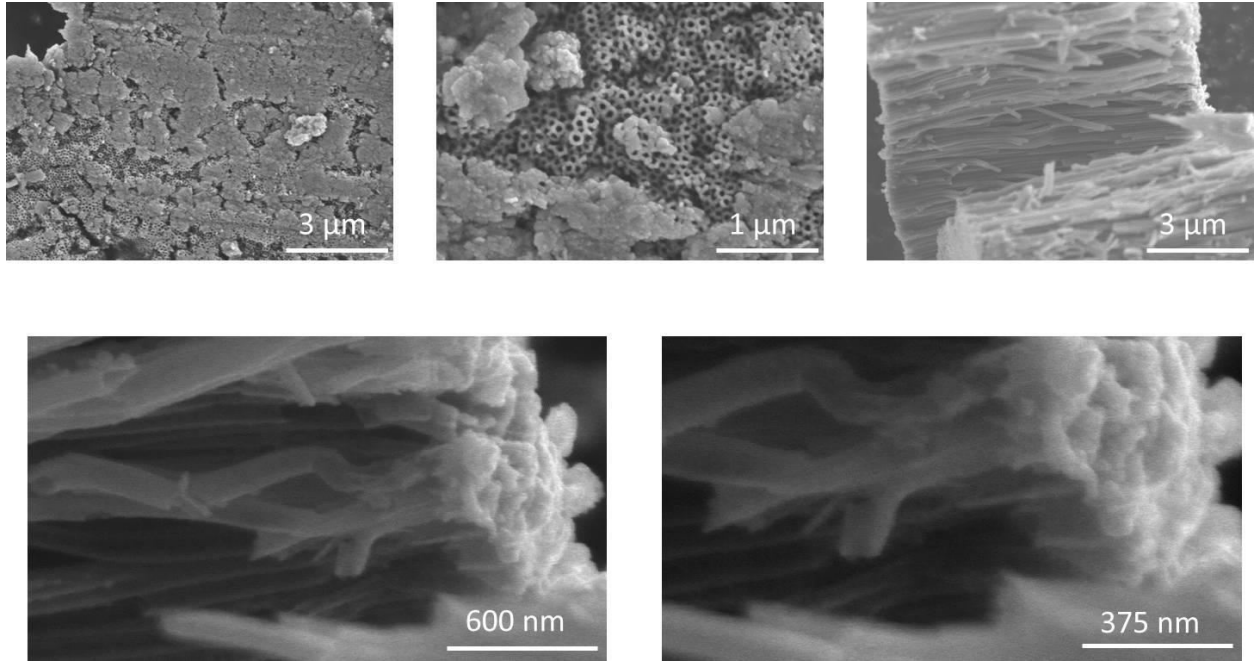
Figure C4. Scanning electron microscope images of photovoltaic devices containing ZnS barrier layer

APPENDIX D

PULSED LASER DEPOSITION OF PbS QUANTUM DOTS

D.1 Characterization

Another option for preventing recombination is to have a complete layer of PbS quantum dots preventing contact from occurring between TiO_2 and the ITO. Exclusion of solvents from the high-aspect ratio nanotubes limits the ability to deposit a complete monolayer of quantum dots using solution-phase methods. An alternative is to use a vapor phase deposition technique, such as evaporation of a single-source precursor into the nanotubes and subsequent decomposition of the precursor using confined plume chemical deposition[109].

Diethyldithiocarbamatolead(II)[110] was evaporated into the nanotubes by gently heating the pre-cursor powder to above 200°C in a 3-neck flask. The evaporated pre-cursor is swept by Ar gas flow into a side-arm flask that contains the nanotube array. The pre-cursor cools and deposits within the nanotube array. Once the pre-cursor is deposited, the nanotube array is subjected to laser irradiation (Er:YAG, λ=2.94 μm, E= 100 mJ, ν= 20 Hz, pulse duration= 150 μs). The laser was focused through a cylindrical ZnSe lens and rastered 5 times across the surface of the substrate at a rate of 317 um/s. The laser irradiation and confinement creates a localized plasma plume that has temperatures around 3000 K. Within the plume, the pre-cursor decomposes to produce PbS quantum dots, as shown in Figure D1.
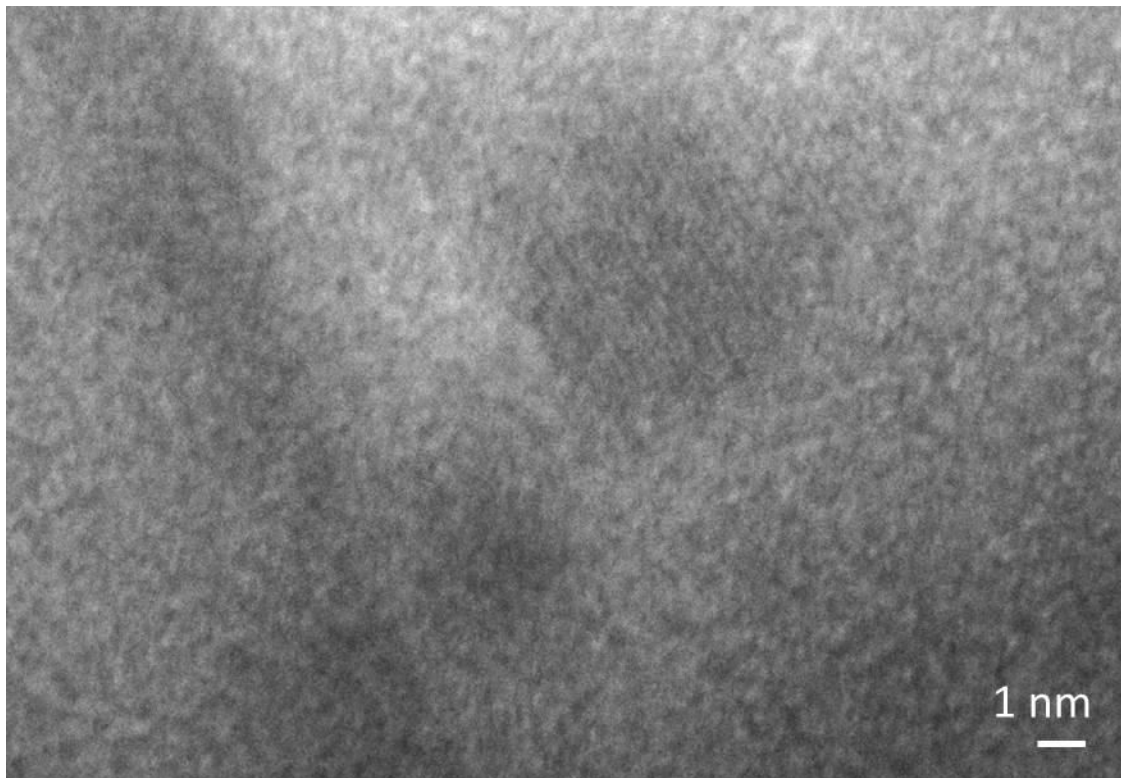
Figure D1. Transmission electron microscope image of PbS quantum dots synthesized within a TiO$_2$ nanotube using confined plume chemical deposition

While the lasing did produce quantum dots, it severally damaged the nanotube array as seen in the photograph and scanning electron microscope images shown in Figure D2. The damage to the nanotube array prevented further use of these substrates for photovoltaic devices.
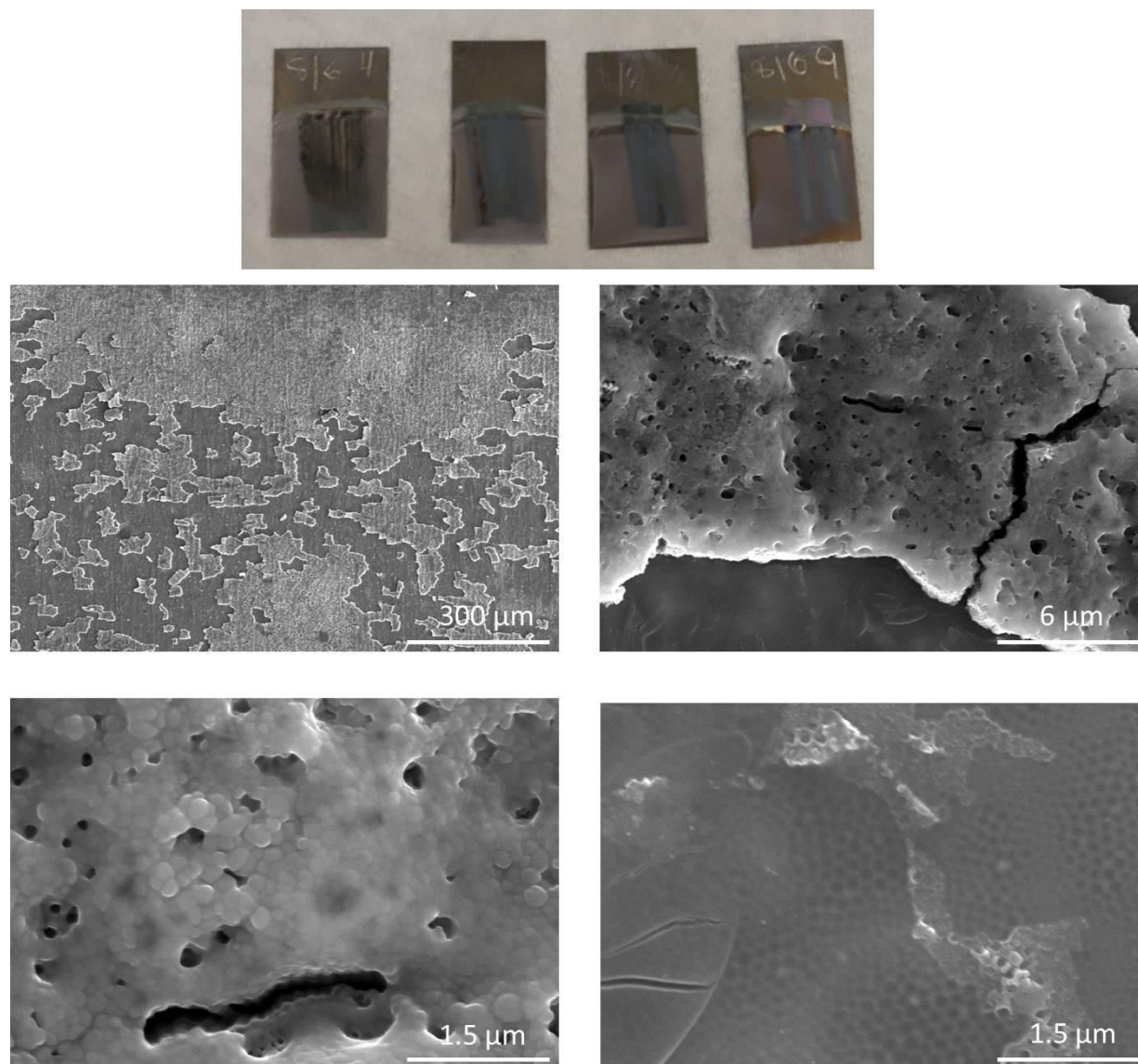
Figure D2. Photograph (top) and scanning electron microscope images (bottom) of damage caused by laser irradiation of nanotube array during confined plume chemical deposition of PbS

REFERENCES

1.   Scholes, G. D.; Rumbles, G., Excitons in Nanoscale Systems. *Nature Materials* **2006,** *5* (9), 683-696.

2.   Efros, A. L.; Rosen, M.; Kuno, M.; Nirmal, M.; Norris, D. J.; Bawendi, M., Band-edge Exciton in Quantum Dots of Semiconductors with a Degenerate Valence Band: Dark and Bright Exciton States. *Physics Review B: Condensed Matter* **1996,** *54* (7), 4843-4856.

3.   Brus, L. E., Electron-Electron and Electron-Hole Interactions in Small Semiconductor Crystallites: The Size Dependence of the Lowest Excited Electronic State. *Journal of Chemical Physics* **1984,** *80* (9), 4403-4409.

4.   Luque, A.; Hegedus, S.; Editors, *Handbook of Photovoltaic Science and Engineering*. John Wiley & Sons Ltd.: 2003; p 1138 .

5.   Cahen, D.; Hodes, G.; Grätzel, M.; Guillemoles, J. F.; Riess, I., Nature of Photovoltaic Action in Dye-Sensitized Solar Cells. *The Journal of Physical Chemistry B* **2000,** *104* (9), 2053-2059.

6.   Peng, J.; Lu, L.; Yang, H., Review on Life Cycle Assessment of Energy Payback and Greenhouse Gas Emission of Solar Photovoltaic Systems. *Renewable and Sustainable Energy Reviews* **2013,** *19* (0), 255-274.

7.   Swafford, L. A.; Rosenthal, S. J. In *Molecular- and Nanocrystal-Based Photovoltaics*, American Scientific Publishers: 2003; p 263-290.

8.   Leblanc, G.; Gizzie, E.; Yang, S.; Cliffel, D. E.; Jennings, G. K., Photosystem I Protein Films at Electrode Surfaces for Solar Energy Conversion. *Langmuir* **2014,** 10.1021/la5010616.

9.   O'Regan, B.; Grätzel, M., A Low-Cost, High-Efficiency Solar Cell Based on Dye-Sensitized Colloidal TiO_2 Films. *Nature* **1991,** *353* (24), 737-740.

10.   Fishman, O. S., Solar Silicon: Part II. *Advanced Material Processes* **2008,** *166* (10), 33-34.

11.   Hemlock Semiconductor Corporation and Hemlock Semiconductor, L. L. C. Energy Rates and the Future of Manufacturing in Michigan.
http://www.michigan.gov/documents/energy/HSC_413569_7.pdf (accessed July 14, 2014).

12.   Lide, D. R., editor; *CRC Handbook of Chemistry and Physics*. CRC Press: Boca Raton, Fla., 1998.

13.   Shockley, W.; Queisser, H. J., Detailed Balance Limit of Efficiency of p-n Junction Solar Cells. *Journal of Applied Physics* **1961,** *32*, 510-19.

14.   Yahyaie, I.; McEleney, K.; Walter, M.; Oliver, D. R.; Thomson, D. J.; Freund, M. S.; Lewis, N. S., Electrical Characterization of Si Microwires and of Si Microwire/Conducting Polymer Composite Junctions. *Journal of Physical Chemistry Letters* **2011,** *2* (6), 675-680.

15.   Verlinden, P. J.; Blakers, A. W.; Weber, K. J.; Babaei, J.; Everett, V.; Kerr, M. J.; Stuckings, M. F.; Gordeev, D.; Stocks, M. J., Sliver® solar cells: A New Thin-Crystalline Silicon Photovoltaic Technology. *Solar Energy Materials and Solar Cells* **2006,** *90* (18–19), 3422-3430.

16.   Kissinger, G.; Pizzini, S.; Yamada-Kaneta, H.; Kang, J., Preface: Advanced Silicon Materials Research for Electronic and Photovoltaic Applications. *Physics Status Solidi C* **2012,** *9* (10-11), 1865-1867.

17.   Richards, B. S., Enhancing the Performance of Silicon Solar Cells via the Application of Passive Luminescence Conversion Layers. *Solar Energy Materials & Solar Cells* **2006,** *90* (15), 2329-2337.

18.   Kalowekamo, J.; Baker, E., Estimating the Manufacturing Cost of Purely Organic Solar Cells. *Solar Energy* **2009,** *83* (8), 1224-1231.

19.   Nazeeruddin, M.; Pechy, P.; Renouard, T.; Zakeeruddin, S.; Humphry-Baker, R.; Comte, P.; Liska, P.; Cevey, L.; Costa, E.; Shklover, V.; Spiccia, L.; Deacon, G.; Bignozzi, C.; Grätzel, M., Engineering of Efficient Panchromatic Sensitizers for Nanocrystalline TiO_2-Based Solar Cells. *Journal of American Chemistry Society* **2001,** *123*, 1613-1624.

20.   Grätzel, M., Conversion of Sunlight to Electric Power by Nanocrystalline Dye-Sensitized Solar Cells. *Journal of Photochemistry & Photobiology A* **2004,** *164*, 3-14.

21.   Yang, D.; Park, H.; Cho, S.; Kim, H.; Choi, W., TiO_2-Nanotube-Based Dye-Sensitized Solar Cells Fabricated by an Efficient Anodic Oxidation for High Surface Area. *Journal of Physical Chemistry Solids* **2008,** *69*, 1272-1275.

22.   Goh, C.; Coakley, K.; McGehee, M., Nanostructing Titania by Embossing with Polymer Molds Made from Anodic Alumina Templates. *Nano Letters* **2005,** *5* (8), 1545-1549.

23.   Gong, D.; Grimes, C.; Varghese, O.; Hu, W.; Singh, R.; Chen, Z.; Dickey, E., Titanium Oxide Nanotube Arrays Prepared by Anodic Oxidation. *Journal of Materials Research* **2001,** *16*, 3331-3334.

24.   Nakayama, K.; Kubo, T.; Tsubokura, A.; Nishikitani, Y.; Masuda, H., Anodic Formation of High-Aspect-Ratio Titania Nanotubes. *ECS Meeting Abstracts* **2006,** *502*, 819.

25.   Richter, C.; Panaitescu, E.; Willey, R.; Menon, L., Titania Nanotubes Prepared by Anodization in Fluorine-Free Acids. *Journal of Materials Research* **2007,** *22*, 1624-1631.

26.   Zaban, A.; Greeensheit, M.; Bisquert, J., Determination of the Electron Lifetime in Nanocrystalline Dye Solar Cells by Open-Circuit Voltage Decay Measurements. *Chemistry & Physical Chemistry* **2003,** *4*, 859-864.

27.   **Solarnix** Iodolyte HI-30 MSDS. http://www.solaronix.com/msds/MSDS_Iodolyte_HI-30.pdf (accessed 08.08).

28.   Hodes, G., Comparison of Dye- and Semiconductor-Sensitized Porous Nanocrystalline Liquid Junction Solar Cells. *Journal of Physical Chemistry C* **2008,** *112* (46), 17778-17787.

29.   Erwin, M. M.; Kadavanich, A. V.; McBride, J.; Kippeny, T.; Pennycook, S.; Rosenthal, S. J., Material Characterization of a Nanocrystal Based Photovoltaic Device. *European Physical Journal D* **2001,** *16* (1-3), 275-277.

30.   Fang, Z.; Eshbaugh, A. A.; Schanze, K. S., Low-Bandgap Donor-Acceptor Conjugated Polymer Sensitizers for Dye-Sensitized Solar Cells. *Journal of American Chemistry Society* **2011,** *133* (9), 3063-3069.

31.   Bai, Y.; Cao, Y.; Zhang, J.; Wang, M.; Li, R.; Wang, P.; Zakeeruddin, S. M.; Gratzel, M., High-Performance Dye-Sensitized Solar Cells Based on Solvent-Free Electrolytes Produced from Eutectic Melts. *Nature Materials* **2008,** *7* (8), 626-630.

32.   Natu, G.; Hasin, P.; Huang, Z.; Ji, Z.; He, M.; Wu, Y., Valence Band-Edge Engineering of Nickel Oxide Nanoparticles via Cobalt Doping for Application in p-Type Dye-Sensitized Solar Cells. *ACS Applied Materials & Interfaces* **2012,** *4* (11), 5922-5929.

33.   Kothe, T.; Poeller, S.; Zhao, F.; Fortgang, P.; Roegner, M.; Schuhmann, W.; Plumere, N., Engineered Electron-Transfer Chain in Photosystem 1 Based Photocathodes Outperforms Electron-Transfer Rates in Natural Photosynthesis. *European Journal of Chemistry* **2014,** *20* (35), 11029-11034.

34.   Shao, C.; Meng, X.; Jing, P.; Sun, M.; Zhao, J.; Li, H., Enhancement of Electron Transfer from CdSe Core/Shell Quantum Dots to TiO_2 Films by Thermal Annealing. *Journal of Luminesence* **2013,** *142*, 196-201.

35.   Underwood, D. F.; Kippeny, T.; Rosenthal, S. J., Charge Carrier Dynamics in CdSe Nanocrystals: Implications for the Use of Quantum Dots in Novel Photovoltaics. *European Journal of Physics D* **2001,** *16* (1-3), 241-244.

36.   Mittleman, D. M.; Rosenthal, S. J.; Schoenlein, R. W.; Yeh, A. T.; Shank, C. V.; Shiang, J. J.; Colvin, V. L.; Grubbs, R. A.; Alivisatos, A. P., Ultrafast Dynamics in CdSe Nanocrystals. *Springer Services Chemistry and Physics* **1994,** *60* (Ultrafast Phenomena IX), 351-3.

37.   Hoheisel, W.; Colvin, V. L.; Johnson, C. S.; Alivisatos, A. P., Threshold for Quasicontinuum Absorption and Reduced Luminescence Efficiency in CdSe Nanocrystals. *Journal of Chemistry & Physics* **1994,** *101* (10), 8455-60.

38.   Blanton, S. A.; Leheny, R. L.; Hines, M. A.; Guyot-Sionnest, P., Dielectric Dispersion Measurements of CdSe Nanocrystal Colloids: Observation of a Permanent Dipole Moment. *Physical Review Letters* **1997,** *79* (5), 865-868.

39.   Dimitriev, O. P.; Kislyuk, V. V.; Syngaevsky, A. F.; Smertenko, P. S.; Pud, A. A., Different Roles of Cadmium- and Sulfur (Selenium)-Terminated Crystal Facets in the Formation of a Photovoltaic Response from Hybrid Organic/Inorganic CdS (CdSe) Heterojunctions. *Physics Status Solidi A* **2009,** *206* (11), 2645-2651.

40.   Fleming, G. R.; Scholes, G. D., Physical Chemistry: Quantum Mechanics for Plants. *Nature* **2004,** *431* (7006), 256-7.

41.   Gao, J.; Perkins, C. L.; Luther, J. M.; Hanna, M. C.; Chen, H.-Y.; Semonin, O. E.; Nozik, A. J.; Ellingson, R. J.; Beard, M. C., n-Type Transition Metal Oxide as a Hole Extraction Layer in PbS Quantum Dot Solar Cells. *Nano Letters* **2011,** *11* (8), 3263-3266.

42.   Allam, N. K.; Shankar, K.; Grimes, C. A., A General Method for the Anodic Formation of Crystalline Metal Oxide Nanotube Arrays Without the Use of Thermal Annealing. *Advanced Materials* **2008,** *20*, 3942-3946.

43.   Smith, N. J.; Emmett, K. J.; Rosenthal, S. J., Photovoltaic Cells Fabricated by Electrophoretic Deposition of CdSe Nanocrystals. *Applied Physics Letters* **2008,** *93* (4), 043504/1-043504/3.

44.   Robel, I.; Subramanian, V.; Kuno, M.; Kamat, P. V., Quantum Dot Solar Cells. Harvesting Light Energy with CdSe Nanocrystals Molecularly Linked to Mesoscopic TiO_2 Films. *Journal of American Chemistry Society* **2006,** *128* (7), 2385-2393.

45.   Kang, Q.; Liu, S.; Yang, L.; Cai, Q.; Grimes, C. A., Fabrication of PbS Nanoparticle-Sensitized TiO_2 Nanotube Arrays and Their Photoelectrochemical Properties. *ACS Applied Materials and Interfaces* **2011,** *3* (3), 746-749.

46.   Kovtyukhova, N. I.; Mallouk, T. E., Conductive Indium-Tin Oxide Nanowire and Nanotube Arrays Made by Electrochemically Assisted Deposition in Template Membranes: Switching Between Wire and Tube Growth Modes by Surface Chemical Modification of the Template. *Nanoscale* **2011,** *3* (4), 1541-1552.

47.   Kovtyukhova, N. I.; Mallouk, T. E., Electrochemically Assisted Deposition as a New Route to Transparent Conductive Indium Tin Oxide Films. *Chemistry of Materials* **2010,** *22* (17), 4939-4949.

48.   Zhang, Z.; Zhou, F.; Lavernia, E. J., On the Analysis of Grain Size in Bulk Nanocrystalline Materials via X-ray Diffraction. *Metallurgical Materials Transactions A* **2003,** *34A* (6), 1349-1355.

49.   Feng, L.; Li, S.; Li, Y.; Li, H.; Zhang, L.; Zhai, J.; Song, Y.; Liu, B.; Jiang, L.; Zhu, D., Super-Hydrophobic Surfaces: From Natural to Artificial. *Advanced Materials* **2002,** *14* (24), 1857-1860.

50.   Erbil, H. Y.; Demirel, A. L.; Avci, Y.; Mert, O., Transformation of a Simple Plastic into a Superhydrophobic Surface. *Science* **2003,** *299* (5611), 1377-1380.

51.   Shang, H. M.; Wang, Y.; Takahashi, K.; Cao, G. Z.; Li, D.; Xia, Y. N., Nanostructured Superhydrophobic Surfaces. *Journal of Materials Science* **2005,** *40* (13), 3587-3591.

52.   Fallah, H. R.; Ghasemi, M.; Hassanzadeh, A.; Steki, H., The Effect of Annealing on Structural, Electrical and Optical Properties of Nanostructured ITO Films Prepared by e-beam Evaporation. *Materials Research Bulletin* **2007,** *42* (3), 487-496.

53.   Chang, R., *Chemistry*. McGraw-Hill Companies,Incorporated: 2009.

54.   Toyoda, T.; Shen, Q., Quantum-Dot-Sensitized Solar Cells: Effect of Nanostructured TiO$_2$ Morphologies on Photovoltaic Properties. *Journal of Physical Chemistry Letters* **2012,** *3* (14), 1885-1893.

55.   Chuang, C.-H. M.; Brown, P. R.; Bulovic, V.; Bawendi, M. G., Improved Performance and Stability in Quantum Dot Solar Cells Through Band Alignment Engineering. *Nature Materials* **2014**, *13,* 796-801.

56.   Ko, D.-K.; Brown, P. R.; Bawendi, M. G.; Bulovic, V., p-i-n Heterojunction Solar Cells with a Colloidal Quantum-Dot Absorber Layer. *Advanced Materials* **2014,** *26* (28), 4845-4850.

57.   Mora-Sero, I.; Gimenez, S.; Moehl, T.; Fabregat-Santiago, F.; Lana-Villareal, T.; Gomez, R.; Bisquert, J., Factors Determining the Photovoltaic Performance of a CdSe Quantum Dot Sensitized Solar Cell: The Role of the Linker Molecule and of the Counter Electrode. *Nanotechnology* **2008,** *19* (42), 424007/1-424007/7.

58.   Shalom, M.; Ruhle, S.; Hod, I.; Yahav, S.; Zaban, A., Energy Level Alignment in CdS Quantum Dot Sensitized Solar Cells Using Molecular Dipoles. *Journal of American Chemistry Society* **2009,** *131* (29), 9876-9877.

59.   Brown, P. R.; Kim, D.; Lunt, R. R.; Zhao, N.; Bawendi, M. G.; Grossman, J. C.; Bulovic, V., Energy Level Modification in Lead Sulfide Quantum Dot Thin Films through Ligand Exchange. *ACS Nano* **2014**, *8*(6), 5863-5872.

60.   Alivisatos, A. P., Nanocrystals: Building Blocks for Modern Materials Design. *Endeavour* **1997,** *21* (2), 56-60.

61.   Lan, X.; Masala, S.; Sargent, E. H., Charge-Extraction Strategies for Colloidal Quantum Dot Photovoltaics. *Nature Materials* **2014,** *13* (3), 233-240.

62.   Garrett, M. D.; Dukes, A. D., III; McBride, J. R.; Smith, N. J.; Pennycook, S. J.; Rosenthal, S. J., Band Edge Recombination in CdSe, CdS and CdSxSe1-x Alloy Nanocrystals Observed by Ultrafast Fluorescence Upconversion: The Effect of Surface Trap States. *Journal of Physical Chemistry C* **2008,** *112* (33), 12736-12746.

63.   Kamat, P. V., Quantum Dot Solar Cells. The Next Big Thing in Photovoltaics. *Journal of Physical. Chemistry Letters* **2013,** *4* (6), 908-918.

64.   Santra, P. K.; Kamat, P. V., Tandem-Layered Quantum Dot Solar Cells: Tuning the Photovoltaic Response with Luminescent Ternary Cadmium Chalcogenides. *Journal of American Chemistry Society* **2013,** *135* (2), 877-885.

65.   Green, M. A., Prospects for Photovoltaic Efficiency Enhancement Using Low-Dimensional Structures. *Nanotechnology* **2000,** *11* (4), 401-405.

66.   Kirmani, A. R.; Carey, G. H.; Abdelsamie, M.; Yan, B.; Cha, D.; Rollny, L. R.; Cui, X.; Sargent, E. H.; Amassian, A., Effect of Solvent Environment on Colloidal-Quantum-Dot Solar-Cell Manufacturability and Performance. *Advanced Materials* **2014**, *26* (27), 4717-4723.

67.   Arango, A. C.; Oertel, D. C.; Xu, Y.; Bawendi, M. G.; Bulovic, V., Heterojunction Photovoltaics Using Printed Colloidal Quantum Dots as a Photosensitive Layer. *Nano Letters* **2009,** *9* (2), 860-863.

68.   Lewis, N. S.; Nocera, D. G., Powering the Planet: Chemical Challenges in Solar Energy Utilization. *Proceedings of National Academy of Science U. S. A.* **2007,** *104* (50), 20142.

69.   Varghese, J.; Whatmore, R. W.; Holmes, J. D., Ferroelectric Nanoparticles, Wires and Tubes: Synthesis, Characterisation and Applications. *Journal of Materials Chemistry C* **2013,** *1* (15), 2618-2638.

70.   Cross, L. E.; Newnham, R. E., History of Ferroelectrics. *Ceramics Civilization* **1986,** *3* (High-Technol. Ceram.), 289-305.

71.   Garbovskiy, Y.; Zribi, O.; Glushchenko, A. In *Emerging Applications of Ferroelectric Nanoparticles in Materials Technologies, Biology and Medicine,* InTech: 2013; pp 475-497.

72.   Scott, J. F., Applications of Modern Ferroelectrics. *Science* **2007,** *315* (5814), 954-959.

73.   Beberwyck, B. J.; Surendranath, Y.; Alivisatos, A. P., Cation Exchange: A Versatile Tool for Nanomaterials Synthesis. *Journal of Physical Chemistry C* **2013,** *117* (39), 19759-19770.

74.   Sun, X.; Huang, X.; Guo, J.; Zhu, W.; Ding, Y.; Niu, G.; Wang, A.; Kiesewetter, D. O.; Wang, Z. L.; Sun, S.; Chen, X., Self-Illuminating ^{64}Cu-Doped CdSe/ZnS Nanocrystals for *In Vivo* Tumor Imaging. *Journal of American Chemistry Society* **2014,** *136* (5), 1706-1709.

75.   Masumdar, E. U.; Gaikwad, V. B.; Pujari, V. B.; More, P. D.; Deshmukh, L. P., Some Studies on Chemically Synthesized Antimony-Doped CdSe Thin Films. *Materials, Chemistry and Physics* **2003,** *77* (3), 669-676.

76.   Costas-Mora, I.; Romero, V.; Lavilla, I.; Bendicho, C., Solid-State Chemiluminescence Assay for Ultrasensitive Detection of Antimony Using On-Vial Immobilization of CdSe Quantum Dots Combined with Liquid-Liquid-Liquid Microextraction. *Analytica Chimica Acta* **2013,** *788*, 114-121.

77.   Dirin, D. N.; Dreyfuss, S.; Bodnarchuk, M. I.; Nedelcu, G.; Papagiorgis, P.; Itskos, G.; Kovalenko, M. V., Lead Halide Perovskites and Other Metal Halide Complexes As Inorganic Capping Ligands for Colloidal Nanocrystals. *Journal of American Chemistry Society* **2014,** *136* (18), 6550-6553.

78.   Previous literature consisting of the 10,316 references for CdSe quantum dots and 6,662 references for SbCl$_3$ as reported on SciFinder® as of June 18, 2014.

79.   Jin, R.; Chen, G.; Xu, H.; Chen, D., Solvothermal Synthesis and Growth Mechanism of Sb$_2$Se$_3$ Nanoplates with Electrochemical Hydrogen Storage Ability. *International Journal of Hydrogen Energy* **2013,** *38* (25), 10971-10977.

80.   Zhai, T.; Ye, M.; Li, L.; Fang, X.; Liao, M.; Li, Y.; Koide, Y.; Bando, Y.; Golberg, D., Single-Crystalline Sb$_2$Se$_3$ Nanowires for High-Performance Field Emitters and Photodetectors. *Advanced Materials* **2010,** *22* (40), 4530-4533.

81.   Ma, J.; Wang, Y.; Wang, Y.; Chen, Q.; Lian, J.; Zheng, W., Controlled Synthesis of One-Dimensional Sb$_2$Se$_3$ Nanostructures and Their Electrochemical Properties. *Journal of Physical Chemistry C* **2009,** *113* (31), 13588-13592.

82.   Bowen, C. R.; Kim, H. A.; Weaver, P. M.; Dunn, S., Piezoelectric and Ferroelectric Materials and Structures for Energy Harvesting Applications. *Energy Environmental Science* **2014,** *7* (1), 25-44.

83.   Tadigadapa, S., Piezoelectric Microelectromechanical Systems - Challenges and Opportunities. *Procedia Engineering* **2010,** *5*, 468-471.

84.   Aghamalyan, N. R.; Aslanyan, T. A.; Vardanyan, E. S.; Kafadaryan, E. A.; Hovsepyan, R. K.; Petrosyan, S. I.; Poghosyan, A. R., Ferroelectric Field-Effect Transistor Based on ZnO:Li/LiNbO$_3$ and ZnO:Li/TGS Heterostructures for IR Pyrodetectors. *Journal of Contemporary Physics* **2013,** *48* (2), 93-97.

85.   Karpov, V. G.; Shvydka, D., Pyroelectric Coupling in Thin Film Photovoltaics. *Physica Status Solidi RRL* **2007,** *1* (4), 132-134.

86.   Seidell, A., *Solubilities of Inorganic and Organic Compounds: A Compilation of Quantitative Solubility Data from the Periodical Literature*. D.Van Nostrand Company: 1919.

87.   Basun, S. A.; Cook, G.; Reshetnyak, V. Y.; Glushchenko, A. V.; Evans, D. R., Dipole Moment and Spontaneous Polarization of Ferroelectric Nanoparticles in a Nonpolar Fluid Suspension. *Physics Review B: Condensed Matter and Materials Physics* **2011,** *84* (2), 024105/1-024105/8.

88.   Yu, W. W.; Qu, L.; Guo, W.; Peng, X., Experimental Determination of the Extinction Coefficient of CdTe, CdSe, and CdS Nanocrystals. *Chemistry of Materials* **2003,** *15* (14), 2854-2860.

89.   Khanna, P. K.; Srinivasa Rao, K.; Patil, K. R.; Singh, V. N.; Mehta, B. R., One-Pot Synthesis of Oleic Acid-Capped Cadmium Chalcogenides (CdE: E = Se, Te) Nano-crystals. *Journal of Nanoparticle Research* **2010,** *12* (1), 101-109.

90.   Dawar, R.; Pankajavalli, R.; Joseph, J.; Anthonysamy, S.; Ganesan, V., Thermodynamic Characterization of Chromium Tellurate. *Journal of Thermal Analytical Calorimetry* **2013,** *112* (1), 95-102.

91.   Wang, C.; Jin, K.-j.; Xu, Z.-t.; Wang, L.; Ge, C.; Lu, H.-b.; Guo, H.-z.; He, M.; Yang, G.-z., Switchable Diode Effect and Ferroelectric Resistive Switching in Epitaxial $BiFeO_3$ Thin Films. *Applied Physics Letters* **2011,** *98* (19), 192901/1-192901/3.

92.   Zhang, H., Polarization Rotation Theory for Field-Induced-Phase Transitions in $BaTiO_3$ Single Crystal. *Condensed Matter* **2012**, 1-18.

93.   Ricinschi, D.; Kanashima, T.; Okuyama, M., First Principles Study of Tetragonality Ratio and Unit-Cell Volume Influence on Spontaneous Polarization of $BaTiO_3$ and $PbTiO_3$. *Zairyo* **2006,** *55* (2), 169-172.

94.   Luby, S.; Cervenak, J.; Kubek, J.; Marcin, M.; Schilder, J., Switching Phenomena in Amorphous Thin Films of Germanium, Cd_xTe_y, and Sb_xSe_y. *Czechoslovokian Journal of Physics* **1971,** *21* (8), 878-89.

95.   Van der Valk, H. J. L.; Haas, C., Anisotropy of Lattice Vibrations of Layered Compounds. *Physica Status Solidi B* **1977,** *80* (1), 321-32.

96.   Schmidt, M. E.; Blanton, S. A.; Hines, M. A.; Guyot-Sionnest, P., Polar CdSe Nanocrystals: Implications for Electronic Structure. *Journal of Chemistry and Physics.* **1997,** *106* (12), 5254-5259.

97.   Weiss, P. S., Mesoscale Science: Lessons from and Opportunities for Nanoscience. *ACS Nano* **2014,** *8* (11), 11025-11026

98.   Casavola, M.; van Huis, M. A.; Bals, S.; Lambert, K.; Hens, Z.; Vanmaekelbergh, D., Anisotropic Cation Exchange in PbSe/CdSe Core/Shell Nanocrystals of Different Geometry. *Chemistry of Materials* **2012,** *24* (2), 294-302.

99.   Allen, P. M.; Harris, D. K.; Bawendi, M. G., In Situ Electrical Monitoring of Cation Exchange in Nanowires. *Nano Letters* **2010,** *10* (10), 3948-3951.

100.   Li, H.; Brescia, R.; Krahne, R.; Bertoni, G.; Alcocer, M. J. P.; D'Andrea, C.; Scotognella, F.; Tassone, F.; Zanella, M.; De Giorgi, M.; Manna, L., Blue-UV-Emitting ZnSe(Dot)/ZnS(Rod) Core/Shell Nanocrystals Prepared from CdSe/CdS Nanocrystals by Sequential Cation Exchange. *ACS Nano* **2012,** *6* (2), 1637-1647.

101.   Li, J.; Zhang, T.; Ge, J.; Yin, Y.; Zhong, W., Fluorescence Signal Amplification by Cation Exchange in Ionic Nanocrystals. *Angewante Chemica International Edition English* **2009,** *48* (9), 1588-91.

102.   Jain, P. K.; Amirav, L.; Aloni, S.; Alivisatos, A. P., Nanoheterostructure Cation Exchange: Anionic Framework Conservation. *Journal of American Chemistry Society* **2010,** *132* (29), 9997-9999.

103.   Shaldin, Y. V.; Matyiasik, S.; Davydov, A. A.; Zhavoronkov, N. V., Pyroelectric Properties of the Wide-Gap CdSe Semiconductor in the Low-Temperature Region. *Semiconductors* **2014,** *48* (1), 1-8.

104.   Wang, D.; Liu, L., Continuous Fabrication of Free-Standing TiO_2 Nanotube Array Membranes with Controllable Morphology for Depositing Interdigitated Heterojunctions. *Chemistry of Materials* **2010,** *22*, 6656-6664.

105.   Park, J. H.; Lee, T.-W.; Kang, M. G., Growth, Detachment and Transfer of Highly-Ordered TiO$_2$ Nanotube Arrays: Use in Dye-Sensitized Solar Cells. *Chemical Communications* **2008,** (25), 2867-2869.

106.   Lin, J.; Chen, J.; Chen, X., High-Efficiency Dye-Sensitized Solar Cells Based on Robust and Both-End-Open TiO$_2$ Nanotube Membranes. *Nanoscale Research Letters* **2011,** *6*, 475.

107.   Mehrabian, M.; Mirabbaszadeh, K.; Afarideh, H., Solid-State ZnS Quantum Dot-Sensitized Solar Cell Fabricated by the Dip-SILAR Technique. *Physica Scripta* **2014,** *89* (8), 085801/1-085801/8.

108.   Liu, C.; Mu, L.; Jia, J.; Zhou, X.; Lin, Y., Boosting the Cell Efficiency of CdSe Quantum Dot Sensitized Solar Cell via a Modified ZnS Post-Treatment. *Electrochimica Acta* **2013,** *111*, 179-184.

109.   Ivanov, B. L.; Wellons, M. S.; Lukehart, C. M., Confined-Plume Chemical Deposition: Rapid Synthesis of Crystalline Coatings of Known Hard or Superhard Materials on Inorganic or Organic Supports by Resonant IR Decomposition of Molecular Precursors. *Journal of American Chemistry Society* **2009,** *131* (33), 11744-11750.

110.   Akhtar, J.; Malik, M. A.; O'Brien, P.; Helliwell, M., Controlled Synthesis of PbS Nanoparticles and the Deposition of Thin Films by Aerosol-Assisted Chemical Vapour Deposition (AACVD). *Journal of Materials Chemistry* **2010,** *20* (29), 6116-6124.